In-flight Air Density Estimation and Prediction for Hypersonic Flight Vehicles

Hamza El-Kebir*
University of Illinois at Urbana-Champaign, IL 61801; and
Delft University of Technology, 2629 HS Delft, The Netherlands

Melkior Ornik†
University of Illinois at Urbana-Champaign, IL 61801

It has been shown that freestream velocity disturbances may cause substantial aeroelastic and aerothermal loading on a hypersonic flight vehicle due to the inadvertent formation of shock waves and rapid changes in air density. We present here a novel state estimation framework to determine and predict the air density acting on a hypersonic flight vehicle. Our approach is comprised of a learning algorithm that updates the air density estimate given observations made by conventional inertial measurement unit sensors earlier on in flight, while exploiting known maximum bounds on acceleration changes and angular rates in the given flight regime. The primary motivation for this research is to enable predictive maneuvering so as to anticipate density perturbations, thereby alleviating aerothermal loads. Previous related work has seen many applications in the field of low speed aeronautics, relying on Kalman and moving average window filters, which suffice only in the case of low frequency changes, require heuristics in tuning them, and are not applicable to the high frequency flow perturbations that are experienced in hypersonic flight. We demonstrate the proposed approach by applying it to the entry trajectory of the Mars Phoenix lander. The atmospheric properties obtained by applying our methodology to this test case are validated using previous trajectory reconstruction efforts and the NASA Mars-GRAM 2010 atmospheric model, allowing for validation of the estimate atmospheric properties generated by the present algorithm.

Nomenclature

Latin symbols

A	=	aerodynamic reference area
a	=	linear acceleration acting on the vehicle
c	=	cosine
C_A	=	force coefficient in the axial direction
$\mathbf{C}$	=	constraint matrix
t_0	=	epoch time
F	=	force acting on the vehicle
f	=	generic function
g	=	gravitational acceleration
h	=	sampling period, or height
H	=	scale height
$\mathbf{I}$	=	identity matrix
k	=	time index
m	=	prediction window length, or mass
n	=	(filtering) window length
N	=	number of filtering windows
p	=	pressure
$\mathbb{P}$	=	probability function
r	=	radius
s	=	sine
t	=	time
V	=	velocity
$\mathbf{R}$	=	rotation matrix
$\mathbb{R}$	=	set of real numbers
$\mathbf{x}$	=	truth vector
$\mathbf{x}^*$	=	filtered truth vector
$\underline{\mathbf{x}}^*$	=	concatenated filtered truth vector
$\mathscr{X}$	=	admissible solution set
$\mathbf{y}$	=	observation vector
$\mathbb{Z}^+$	=	set of positive integers

*Undergraduate Student, Department of Aerospace Engineering
†Assistant Professor, Department of Aerospace Engineering

Greek symbols

α = angle of attack
β = sideslip angle
ε = bound
$\underline{\varepsilon}$ = gradient bound
θ = pitch angle
ϑ = azimuthal angle
$\boldsymbol{\theta}$ = parameter vector
μ = gravitational parameter
ρ = density
σ = standard deviation
ϕ = roll angle
φ = polar angle
$\boldsymbol{\varphi}$ = lagged output data vector
ψ = yaw angle
ω = planetary polar angular velocity
Ω = body angular velocity

Subscripts

a = referenced to wind, or prediction parameter
aero = effect due to aerodynamics
body = referenced to body frame
bulk = effect due to atmospheric bulk motion
gust = effect due to gusts
inert = referenced to inertial frame
i = axis index
r = radial axis
wind = effect due to all winds

I. Introduction

Hypersonic flight vehicles (HFVs) are known to be susceptible to flow field disturbances caused by far-field changes in pressure distribution [1, 2]. In operational flight, conventional atmospheric models rarely provide an accurate model for the rapid changes in both the wind field and air density [2, 3]. Harpold and Gavert [4] and Hale et al. [2] note that significant fluctuations in the angle of attack program of the Space Shuttle Orbiter were measured due to rapid changes in air density, which can be mitigated provided that accurate predictions of density measurements are available. Sustained offsets in the angle of attack can result in the vehicle drifting off of its intended course, thereby over- or undershooting its target destination [5]. To mitigate these effects, many modern atmospheric entry guidance schemes include some model of the density profile to aid in predictive maneuvering during the hypersonic entry phase of a vehicle [6, 7]. Given the fact that atmospheric parameters are known to drastically change as a function of time and position [8, 9], it is often meaningless to utilize the same static air density profiles in a multitude of settings. In the case of the Mars atmosphere, even the highest fidelity models, such as the Mars Global Reference Atmosphere Model 2010 (Mars-GRAM 2010), fail to predict density variations in a number of reported cases [10, 11]. To mitigate this problem, Ding et al. [12] propose the use of a flush air data sensing (FADS) system to aid in the estimation of air data parameters experienced in-flight by a HFV. This approach has been used to great success in many experimental HFVs [13–15], but the data acquired by these sensors requires unbiased noise reduction i.e., filtering. In recent years, HFVs have witnessed an additional development in the field of wind estimation, namely the use of a FADS system, coupled with an inertial measurement unit (IMU) [16].

In general, approaches to density estimation are almost always subsumed in wind estimation schemes, which can be classified in three different categories: a vectorial approach assuming in-plane winds, an approach based on the dynamic response of a flight vehicle, and a combined approach utilizing air data from FADS and the dynamic response [16, 17]. The first of these approaches is heavily reliant on airspeed measurements, as the wind speed is determined by subtracting the ground velocity from the airspeed vector [18–22]. Utilizing this data is cumbersome in the case of HFVs, in part due to the uncertainty of airspeed determined by Pitot tubes in hypersonic flight regimes [23, 24]. Major drawbacks in such schemes, additionally, are rooted in the fact that they rely chiefly on Kalman filters and moving average window filters, which require manual, heuristic, tuning and have previously been optimized for slow variations in wind field [25, 26]. The second approach lies in utilizing inertial measurements made by the autopilot sensors [27]. The primary limitation of using the dynamic response of a vehicle to determine the local wind field is due to the inherent modeling errors in the idealized mathematical model of the vehicle [17, 28]. A possible solution is to determine the vehicle model from flight data, as has previously been in done in *a posteriori* analysis (e.g. [29]); this does, however, require expensive and time-consuming testing campaigns that still leave significant uncertainties in the derived aerodynamic coefficients [30–32]. The final approach, which combines FADS and IMU data, features a number of different implementations. Baumann et al. [14] use complementary filters to smooth the low-frequency FADS flow angles using high-frequency IMU data, only removing noise but not increasing overall prediction accuracy [12].

Karlgaard et al. [16] apply *a posteriori* fitting of the FADS and IMU data using nonlinear weighted least-squares. While most approaches are concerned either with the wind vector or thermodynamic parameters, for full state approaches that estimate both, the Kalman filter seems to be the most commonly used [19, 33, 34]. In this case, however, Kalman filters have the inherent disadvantage of having complex Jacobian matrices that frequently rely on computational fluid dynamics (CFD) simulations, which introduce additional model error [12]. Other approaches are concerned only with the calibration of FADS systems using inertial and meteorological data [35–37], or a posteriori analysis of flight data [33, 34].

As more precise guidance requirements are imposed on modern HFVs, it will prove necessary to determine, on-the-fly, the local atmospheric conditions experienced by the vehicle. To tackle this issue, we propose in Sec. II a novel noise reduction framework known as *change-conscious maximum likelihood estimation* (CCMLE), which allows for efficient online filtering of signals produced through a nonstationary process [38]. Contrary to previous work, CCMLE requires solely knowledge of the maximum expected rate of change of the time series under consideration thus allowing for an intuitive approach to filtering. The maximum rates of change are often known prior to a mission's execution e.g., from engineering specifications or simulations. A novel contribution in this regard is that no knowledge of the HFV dynamics beyond simple inertial properties is required to allow for meaningful estimation. Using this filtered data, we present in Sec. III techniques to compute the approximate wind-relative velocity vector, aerodynamics angles and local atmospheric thermodynamic properties, pressure and density. Since our filter relies on a given number of samples to be known before producing an estimate of the true signal, near-term predictions must be produced to guarantee continuity of important parameters; we propose a simple autoregressive model for m-step-ahead predictions as described in Sec. IV. All of these techniques are then applied to the Mars Phoenix lander mission in Sec. V, demonstrating the online trajectory and atmosphere reconstruction approach presented in this work. We compare our results with the work of Withers and Catling [39], Karlgaard and Tynis [40] and an independently produced atmospheric profile using the Mars Global Reference Atmospheric Model 2010 (Mars-GRAM 2010, [41]). Overall, we observe good agreement between our atmospheric density estimates and those from [39, 40] and the Mars-GRAM 2010 model. Conclusions are drawn in Sec. VI, accompanied by a discussion of the results and future work.

II. Signal Noise Reduction

Before we can consider estimating the atmospheric properties encountered in a vehicle's flight, it is necessary to consider the data that will be used in estimating these parameters. We will mainly focus on inertial measurement unit (IMU) sensor signal, which often have significant noise associated with them [30, 42, 43]. Since we wish to estimate the true signals (i.e., filter out the noise) before we using them to estimate the atmospheric parameters, it becomes necessary to consider which unbiased filtering techniques produce signals suitable for atmosphere reconstruction. In the following, we will review previous noise reduction schemes that have been employed in reconstructing hypersonic entry trajectories, after which we present our own filtering methodology, known as *change-conscious maximum likelihood estimation* (CCMLE). Our discussion will focus chiefly on the properties of past schemes when used in an online setting, which demands that computational strain stays low and samples are quickly processed to produce atmospheric estimates. The proposed CCMLE scheme is formulated for such an online setting, as described hereafter.

A. Previous approaches

Given the need to efficiently and effectively filter time series that are generated by various (noisy) sensors, it becomes necessary to consider suitable online signal processing schemes; before considering these, however, it is instructive to review current trends in offline filtering techniques. In offline trajectory reconstruction, the Kalman filter (KF) and its derivatives, the extended Kalman filter (EKF) and unscented Kalman filter (UKF), have been extensively analyzed in recent years [30, 34, 44, 45]. While the classical discrete-time Kalman filter could be suitable for online use during entry, descent and landing (EDL) considering its performance, it is rarely used in practice due to its linear nature and the highly nonlinear properties of the system dynamics, causing EKF and UKF to be the preferred alternatives [30]. In EKF and UKF, the nonlinear system dynamics are linearized about the current state, and these local linear models are then used to produce filtered estimates. UKF differs from EKF, in that the state transition matrix, which is a Jacobian matrix, need not be calculated analytically, and is therefore more efficient [30]. One major drawback of utilizing any of the Kalman filters, lies in the necessity of a complete description of the system dynamics, which requires the construction of a detailed aerodynamic database and determination of the dynamic and static aerodynamic properties of the vehicle at various flight conditions and orientations [44, 46, 47]. Even after such expensive and time-consuming efforts, an appreciable uncertainty in the vehicle's aerodynamics still remains at the time of EDL [48]. As a result, the Kalman filter

suffers from a lack of robustness stemming from mounting plant–model mismatch, making it ill-suited for application in real-life systems operating under unforgiving circumstances.

Turning to so-called 'model-free' filters, we find that complementary filters are often used in aerospace applications [49, 50]. These filters differ from Kalman filters, as the complementary filter directly combines two or more signals exhibiting low- and high-frequency noise are combined, in the ideal case producing a pure additive white noise signal that is filtered using low- and high-pass filters [49]. Examples of these signals in aerospace applications are descent rates determined from inertial measurements and barometric altimeters, and attitude changes determined from linear accelerations and angular rates measured by gyroscopes [49, 50]. While this approach is computationally tractable, and in simple cases does not require explicit knowledge of the system dynamics, the often fixed nature of the filter gains implies that filter tuning is purely heuristic, and is not receptive to changes in the frequency domain composition of the signal [51]. Another model-free filtering approach found in trajectory reconstruction literature is the moving average window (MAW). Here, the data are smoothed by taking the value of an element to equal the average of a number of samples that lie adjacent to it, i.e. a 'window'. This effectively smoothens the data and suppresses significant gradients from appearing. However, Withers and Catling [39] state that the MAW filter produces biased estimates for linear accelerations experienced during entry, and requires correction to account for the exponential variation of atmospheric density and its multiplicative effects on acceleration. To produce this correction, both a short and long window must be applied, after which the correction is computed by a function involving natural logarithms and powers; in an online setting, this would prove undesirable as it requires the evaluation of computationally demanding functions.

Bearing the above discussion in mind, we propose here a filtering approach adapted from the work of Ornik and Topcu [52]. While the idea of using bounds on the known rate of change of a time-varying function to produce a maximally likely function comes from [52], the approach of [52] applies that idea to Markov decision processes, as opposed to the more general signals that this paper considers. Our approach requires minimal engineering data on the operational constraints of the vehicle, producing online filtered results from any given time series in a batched manner, i.e. the filter is applied after a given number of samples (a window) is accumulated. In the following we will expand on this approach, termed *change-conscious maximum likelihood estimation* (CCMLE).

B. Change-conscious maximum likelihood estimation (CCMLE)

Before stating the mathematical underpinning of the CCMLE [52] methodology, let us consider the following problem: given a noisy signal, and prior knowledge on the dynamics of the true signal, how can we recover an estimate of the true signal? Consider a time series (e.g., a noisy signal) $\mathbf{y}$ containing n samples ($\mathbf{y} \in \mathbb{R}^n$). We assume that each element of this time series is independent and identically distributed (i.i.d.), and is corrupted by a zero-mean Gaussian noise of variance σ^2, which holds over all n samples. Since we will consider a process that is not governed by a stationary (unchanging) noise process, we will assume the time series from which we sample these n to be by a *weakly stationary* process (i.e., the first two moments of the noise process, mean and variance, are constant) [53]. With this assumption, we can assume that the n samples under consideration here are sampled from a stochastically stationary process, which is instrumental to this approach. In practice, this is achieved by either considering high-frequency data sources with frequencies in excess of those of the (noise) process time scale, or we consider processes with a large enough time scale during which samples are considered to originated from an unchanging stochastic process [53].

By assuming any 'window' of n samples that is generated by a stochastically stationary process, we will show that CCMLE produces the most probable estimate of the samples that belongs to some admissible solution set $\mathscr{X}$. This solution set imposes constraints on the problem that allow us to incorporate knowledge of the maximum relative rate of change of the time series, allowing us to pose the underlying optimization problem as a convex optimization problem. Note that the need for windows does not only stem from the fact that the process must be stochastically stationary over the given samples considered, but also because all data are filtered in one pass (a 'batch process'), as opposed to in a recursive manner. Thus, we must wait for a number of samples to be accumulated before they can be filtered and a filtered result is obtained; since we wish to compute estimates of the density online in a timely manner, it is necessary to segment the data and filter smaller windows to quickly obtain a filtered signal without incurring a significant lag.

1. Optimization problem statement

Given a set of observations in the form of a time series, $\mathbf{y} \in \mathbb{R}^n$, we wish to find the set of truths $\mathbf{x} \in \mathbb{R}^n$ such that the likelihood of correctness is maximized, while the truths belong to a domain $\mathscr{X}$ that satisfies a set of linear constraints.

$$\max_{\mathbf{x} \in \mathscr{X}} \mathbb{P}(\mathbf{y} \mid \mathbf{x}). \tag{1}$$

Assuming that observations y_i are independent and identically distributed random variables, we can equivalently express the maximization problem as:

$$\max_{\mathbf{x}\in\mathscr{X}} \mathbb{P}(\mathbf{y} \mid \mathbf{x}) = \max_{\mathbf{x}\in\mathscr{X}} \prod_{i=1}^{n} \mathbb{P}(y_i \mid x_i). \tag{2}$$

Now, we assume that the random variables y_i have a normal distribution centered around the truth with constant standard deviation σ, i.e. $y_i \sim \mathscr{N}(x_i, \sigma^2)$, yielding:

$$\max_{\mathbf{x}\in\mathscr{X}} \prod_{i=1}^{n} \mathbb{P}(y_i \mid x_i) = \max_{\mathbf{x}\in\mathscr{X}} \prod_{i=1}^{n} \frac{1}{\sqrt{2\pi\sigma^2}} \exp\left[-\frac{(y_i - x_i)^2}{2\sigma^2}\right]. \tag{3}$$

Taking the logarithm, which is a monotonically increasing function and thus yields the same maximum, and noting that $1/\sqrt{2\pi\sigma^2}$ is constant, we find:

$$\max_{\mathbf{x}\in\mathscr{X}} \mathbb{P}(\mathbf{y} \mid \mathbf{x}) = \max_{\mathbf{x}\in\mathscr{X}} \log\left\{\prod_{i=1}^{n} \frac{1}{\sqrt{2\pi\sigma^2}} \exp\left[-\frac{(y_i - x_i)^2}{2\sigma^2}\right]\right\} = \max_{\mathbf{x}\in\mathscr{X}} \sum_{i=1}^{n} -\frac{(y_i - x_i)^2}{2\sigma^2} + n\log\left(\frac{1}{\sqrt{2\pi\sigma^2}}\right). \tag{4}$$

We may express this as a minimization problem, giving:

$$\max_{\mathbf{x}\in\mathscr{X}} \mathbb{P}(\mathbf{y} \mid \mathbf{x}) = \min_{\mathbf{x}\in\mathscr{X}} \sum_{i=1}^{n} (x_i - y_i)^2. \tag{5}$$

Expressing this as a bounded variable least squares problem, we find:

$$\min_{\mathbf{x}\in\mathscr{X}} \|\mathbf{x} - \mathbf{y}\|_2^2. \tag{6}$$

This problem is a quadratic programming (QP) problem, which is amenable to efficient numerical solution [54]. Solving for the value $\mathbf{x}^* \in \mathscr{X}$ that minimizes this norm produces the filtered CCMLE time series.

2. Specification of admissible solution set $\mathscr{X}$

In defining the appropriate domain $\mathscr{X}$, we wish to bound the relative change of the truths that we obtain by solving the CCMLE problem; these bounds will originate from knowledge of the underlying physics. In particular, we consider the maximum absolute rate of change between one sample and its previous and subsequent sample. As an example, in the case of a velocity time series, this would be a maximum feasible acceleration, and may be produced from engineering specifications or simulations. Naturally, these bounds are scaled by the sampling period that was applied in obtaining the time series, and may be related to a known continuous time rate of change as follows.

It can be shown that for a time series with constant sampling period, the maximum bound will be equal to the maximum gradient in continuous time multiplied by the sampling period. The bounds are stipulated as part of the admissible solution domain $\mathscr{X}$. Consider the vector of bounds $\boldsymbol{\varepsilon} \in \mathbb{R}^{n-1}$:

$$\boldsymbol{\varepsilon} = \begin{bmatrix} \varepsilon_1 \\ \varepsilon_2 \\ \vdots \\ \varepsilon_{n-1} \end{bmatrix}. \tag{7}$$

The goal is to find $\mathbf{x}$, such that relative rate constraints $|x_i - x_{i-1}| \leq \varepsilon_{i-1}$ for $i \in [2, n]$ are satisfied, while $\mathbf{x}$ is as close as possible to $\mathbf{y}$ (see Eq. 6). We can thus express the constraints imposed by admissible solution set $\mathscr{X}$, by subjecting the minimization problem of Eq. (6) to the following inequality constraint:

$$\mathbf{C}\mathbf{x} \preceq \boldsymbol{\varepsilon}^*, \tag{8}$$

where $\mathbf{C} \in \mathbb{R}^{(2n-2)\times n}$ is a matrix that maps $\mathbf{x}$ such that it satisfies the inequality constraints introduced above using a linear inequality:

$$\mathbf{C} = \begin{bmatrix} 0 & \cdots & \cdots & \cdots & \cdots & \cdots & 0 \\ & 1 & -1 & & & & \\ -1 & 1 & & & & & \\ & & 1 & -1 & & & \\ & -1 & 1 & & & & \\ & & \ddots & \ddots & \ddots & & \\ & & & & & 1 & -1 \\ & & & & -1 & 1 & \\ 0 & \cdots & \cdots & \cdots & \cdots & \cdots & 0 \end{bmatrix}, \tag{9}$$

where the blanks denote zeros, and the first and last row are identically zero; these rows are included for a more coherent structure of the modified bounds vector $\boldsymbol{\varepsilon}^* \in \mathbb{R}^{2n-2}$, which now takes the form:

$$\boldsymbol{\varepsilon}^* = \begin{bmatrix} \varepsilon_1 & \varepsilon_1 & \varepsilon_2 & \varepsilon_2 & \cdots & \varepsilon_k & \varepsilon_k & \cdots & \varepsilon_{n-1} & \varepsilon_{n-1} \end{bmatrix}^\mathsf{T}. \tag{10}$$

3. Concatenation of filtered windows

Assume the n-element observation time series is part of a greater time series, say a time series consisting of N number of n-element windows, as could be the case for a continuous stream of data. This is based on two reasons: one lies in the fact that longer windows will result in increased computational complexity, and become intractable to solve in a short time on modest hardware; the second stems from the fact that we wish to have access to the filtered time series without waiting for data to be accumulated, and additional data cannot be added when the filter is running. Now, ensuring that the concatenated filtering solution, $\underline{\mathbf{x}}^* = (\mathbf{x}_1^*, \ldots, \mathbf{x}_N^*)$, belongs to the compounded admissible solution set, $\mathscr{X}_1 \oplus \ldots \oplus \mathscr{X}_N$, becomes a nontrivial issue. As such, it we propose the following approach: the first unfiltered sample is set to be equal to the first filtered sample through an equality constraint (i.e., $x_1 = y_1$, corresponding to $\varepsilon_1 \equiv 0$ in the above formulation), allowing for the last filtered sample of one window to be taken as the first sample of the next window in practical applications; we employ this approach in subsequent sections. Provided that the sampling rate is high enough, drastic changes between windows on the scale of single elements should not be present, therefore warranting this approach.

4. Numerical solution approach

As could be seen in the foregoing, Eq. (6) presents a constrained quadratic programming (QP) problem [54]. In recent years, many advances in the field of convex and quadratic programming have taken place [55]. This consideration forms an additional advantage to this methodology, as accurate estimates are obtained without the need for heuristics or intensive routines.

In solving the windowed filtering problem in an online setting, we have utilized the CVXGEN software by Mattingley and Boyd [56]. CVXGEN allows for a convex quadratic program to be defined, after which it generates custom library-free and virtually branchless C code, with the explicit intention of its utilization in embedded real-time application [56]. We have successfully leveraged the sparsity of our inequality constraints matrix, allowing for window sizes in excess of 100 samples to be processed without causing deficiencies in the numerical efficiency of the routines in use. CVXGEN makes use of fully iterative procedures, and solves quadratic programming problems using a primal-dual interior point methods, and converges within well under ten iterations for the signals we have studied [56, 57].

Utilization of the generated C code is straightforward, and solely requires definition of the signal elements and bounds vector. While no explicit attempts have been made here at quantifying the (expected) performance on flight hardware, studies have shown that current QP solvers perform well within the microsecond range in industrial settings and produce reliable results [58].

III. Equations of Motion

Having developed a methodology to filter the time series obtained by our sensors, we now wish to use the filtered IMU signals to produce estimates of the atmospheric properties. This requires both *trajectory reconstruction*, and

atmosphere reconstruction, as shown hereafter. We shall base our discussion around trajectory reconstruction approaches as applied in offline settings, allowing for adaptation to online processes. Such methods are widely applied in the analysis of inertial measurements acquired from planetary entry vehicles [39, 44, 59–61]. Below, we present the equations of motion including planetary motion in a planet-fixed rotating coordinated frames, which are then integrated after transformation to an inertial frame [59]. Following the exposition of Withers et al. [59], we shall then present a tested approach to *attitude constraining*. Since there are a number of ways of determining the vehicle attitude in the inertial frame, it is necessary to define a datum and means of determining the rate of change of this attitude, the process of which is known as *attitude constraining*. This step is then followed by atmosphere reconstruction. In this work, we blend the previously *a posteriori* atmospheric reconstruction procedure with the attitude determination step, thereby allowing for atmospheric estimates to be acquired in real time.

A. Motion using accelerometers and gyroscopes

In recent years, virtually all hypersonic vehicles have had linear accelerometers and gyroscopes onboard [30]. In contrast to legacy vehicles, which required extensive use of aerodynamic databases to determine their wind-relative trajectory, the presence of a three-axis gyroscope allows for direct estimation of the wind relative attitude [59]. This methodology precludes the need for an aerodynamic database, and is often used to validate the accuracy of the estimated aerodynamic characteristics of a vehicle post-flight [39, 44, 45, 48, 59].

1. Angular motion

We present the following *attitude-tracking* formulation utilizing gyroscope measurements, based on the work of Withers et al. [59]. Contrasting to the results in [59], we have chosen to employ an intrinsic zyx (yaw-pitch-roll) rotation for our formulation, as outlined in [62, §11.10]:

$$\dot{\psi} = \frac{\Omega_{y,\text{body}} \sin\phi + \Omega_{z,\text{body}} \cos\phi}{\cos\theta} \tag{11a}$$

$$\dot{\theta} = \Omega_{y,\text{body}} \cos\phi - \Omega_{z,\text{body}} \sin\phi \tag{11b}$$

$$\dot{\phi} = \Omega_{x,\text{body}} + \tan\theta \left(\Omega_{y,\text{body}} \sin\phi + \Omega_{z,\text{body}} \cos\phi \right). \tag{11c}$$

Here, ψ, θ, ϕ (yaw, pitch, and roll, respectively) represent the proper Euler angles between the inertial frame and the body (vehicle) frame. The body frame $O_{xyz,\text{body}}$ has x_{body} as its roll axis, y_{body} as its pitch axis, and z_{body} as its yaw axis. Note that this differs from [59], but is in line with more recent trajectory reconstruction efforts and coordinate frame conventions [34, 44, 45, 63]. The $\Omega_{\cdot,\text{body}}$'s represent the angular rates (velocities) about these principal body axes, and are frequently directly output by the inertial measurement after integration of the angular accelerations. The body frame is shown in Fig. 1:

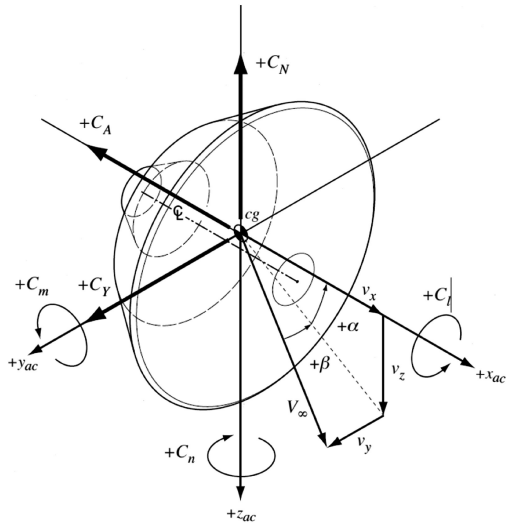

Fig. 1 Body coordinate system [44]

To convert the linear accelerations observed in the body frame, $\mathbf{a}_{\text{aero,body}}$, to the inertial frame, we construct the following rotation matrix, based on the use of proper Euler angles in a roll-pitch-yaw sequence [64, App. A.1]:

$$\mathbf{R}_{\text{body}}^{\text{inert}} = \begin{bmatrix} c_\psi & 0 & s_\psi \\ 0 & 1 & 0 \\ -s_\psi & 0 & c_\psi \end{bmatrix} \begin{bmatrix} c_\theta & -s_\theta & 0 \\ s_\theta & c_\theta & 0 \\ 0 & 0 & 1 \end{bmatrix} \begin{bmatrix} 1 & 0 & 0 \\ 0 & c_\phi & -s_\phi \\ 0 & s_\phi & c_\phi \end{bmatrix} = \begin{bmatrix} c_\theta c_\phi & -c_\phi c_\psi s_\theta + s_\phi s_\psi & c_\psi s_\theta s_\phi + c_\phi s_\psi \\ s_\theta & c_\theta c_\phi & -c_\theta s_\phi \\ -c_\theta s_\psi & c_\psi s_\phi + c_\phi s_\theta s_\psi & c_\phi c_\psi - s_\theta s_\phi s_\psi \end{bmatrix}, \tag{12}$$

where $c_\cdot$ and $s_\cdot$ denote the cosine and sine of the subscript angle, respectively. The inverse rotation, $\mathbf{R}_{\text{inert}}^{\text{body}}$, coincides with the transpose of the above rotation, i.e. $(\mathbf{R}_{\text{body}}^{\text{inert}})^\intercal$. We find the aerodynamic accelerations in the inertial frame as follows:

$$\mathbf{a}_{\text{aero,inert}} = \mathbf{R}_{\text{body}}^{\text{inert}} \mathbf{a}_{\text{aero,body}}. \tag{13}$$

2. Inertial acceleration

Frequently, knowledge of the vehicle's inertial position, velocity and attitude are available at the entry interface is available, and is determined using star trackers, Doppler ranging, or propagation of its state using Keplerian mechanics, or a combination of these [39, 44, 45, 59, 63, 65]. As a result, this instantaneous position is used as the datum for subsequent propagation, and can be related to other inertial reference frames. In order to preclude cumbersome corrections for Coriolis effects and centrifugal forces, we shall consider exclusively the inertial state, which may be transformed at a later stage if desired; this limits the number of computations required substantially [59].

To compute the inertial accelerations, we must add the gravitational acceleration g to the aerodynamic acceleration obtained by the accelerometers. While it is possible to utilize spatial (or spatio-temporal) gravitational models based on spherical harmonics (e.g., MRO110C [66]), we shall consider solely an idealized spherical planetary model in an effort to alleviate computational strain, yielding an inverse-square law gravity field. As such, the gravitational acceleration is only dependent on the radial distance from the planet's center of mass, giving the following gravitational model:

$$g(r) = \frac{\mu}{r^2} = \frac{GM}{r^2}, \tag{14}$$

where μ is the gravitational parameter of the celestial body, which is equal to the product of the universal gravitational constant G, and the mass of the greater body M. Note that it would have been possible to account for oblateness effects (J_2-effects), but this is easily added to the model if the reader so wishes.

This radial acceleration can be converted to the Cartesian inertial frame using the following transformation:

$$\mathbf{g}(x, y, z) = -\begin{bmatrix} \sin\vartheta\cos\varphi \\ \sin\vartheta\sin\varphi \\ \cos\vartheta \end{bmatrix} g(r), \tag{15}$$

where $O_{r\vartheta\varphi}$ denotes the inertial spherical coordinate frame. Summing all accelerations, we obtain:

$$\mathbf{a}_{\text{inert}} = \mathbf{g} + \mathbf{a}_{\text{aero,inert}}. \tag{16}$$

Since the center of mass acceleration of the vehicle is $\ddot{\mathbf{x}} = \mathbf{a}_{\text{inert}}$, integrating both sides of the differential equation twice over time will yield the current vehicle position and velocity in the inertial frame, as propagated from the initial (entry) state discussed before.

Having obtained the vehicle's inertial state and attitude, we can use these results to reconstruct the atmospheric profile, as presented in the next subsections.

B. Atmosphere reconstruction

To determine the atmospheric properties, we must first find the magnitude of the wind-relative velocity. Using the wind-relative velocity vector, we may both define the aerodynamic orientation and the density profile, as outlined below.

1. Wind-relative velocity

While determining the wind direction is straightforward, estimating the wind-relative velocity requires some more insight. Since we are only working with the inertial state, we must account for the bulk atmospheric motion due to the body's rotation, since that makes for the greatest discrepancy between the relative and absolute velocity. In essence, we decompose the inertial velocity vector into three constituents:

$$\mathbf{V}_{\text{inert}} = \mathbf{V}_a + \mathbf{V}_{\text{wind,bulk}} + \mathbf{V}_{\text{wind,gust}}. \tag{17}$$

The bulk atmospheric motion $\mathbf{V}_{\text{wind,bulk}}$ is solely a function of the planetary rate of rotation and the vehicle's location, and is computed as [59]:

$$\mathbf{V}_{\text{wind,bulk}} = \omega\hat{\mathbf{z}} \times \mathbf{x} = \omega \begin{bmatrix} -y \\ x \\ 0 \end{bmatrix}, \tag{18}$$

where ω denotes the angular velocity of the celestial body, $\hat{\mathbf{z}}$ denotes the unit vector in z-direction in the inertial frame, and $\mathbf{x}$ denotes the inertial position vector. Since in practice external measurements are required to determine the wind field we shall assume the gusts to be insignificant. This assumption holds throughout the hypersonic regime [67]. Therefore, we find:

$$\mathbf{V}_a \approx \mathbf{V}_{\text{inert}} - \mathbf{V}_{\text{wind,bulk}}. \tag{19}$$

The above model incorporates the classical assumption that a planet's atmosphere rotates with the same velocity as its core, while extending it with the presence of gusts that are not accounted for in classical formulations [59, 68]. King-Hele and Allan [69] have shown that such an assumption of mean bulk motion holds for the uppermost strata of the Earth's atmosphere, and it would serve as a means of separating a near-constant mean wind from changing gusts, as attempted in the above formulation.

While the body-referenced aerodynamic acceleration already provides us with the direction of the resultant aerodynamic force, it is useful to compute the aerodynamic angles, namely the angle of attack (α) and the sideslip angle (β), which dependent on the body-relative (incident) wind direction. Let us define the unit vector in the direction of the wind-relative velocity in the body frame as:

$$\boldsymbol{\alpha} = \frac{\mathbf{V}_{a,\text{body}}}{\left\|\mathbf{V}_{a,\text{body}}\right\|}. \tag{20}$$

Note that we cannot immediately apply the body-relative acceleration ($\mathbf{a}_{\text{aero,body}}$), as the direction of the resultant vector does not correspond to the wind-relative velocity vector per se. Instead, using the definition of the wind-relative velocity, we find it provides an accurate description of the aerodynamic angles [19, 70]. From the orientation of $\boldsymbol{\alpha}$ and the body x-axis, the aerodynamic angles can be determined as described in, e.g. [70].

2. Atmosphere in the rarefied flow regime

Since the acceleration time series are measured in a vehicle-relative frame, only accelerations due to aerodynamics are observed, given a pure (or filtered) time series. It is then straightforward to relate the observed acceleration to the dynamic pressure and reference area as follows [71]:

$$F_{x,\text{aero}} = ma_x = -\frac{1}{2}\rho V_a^2 A C_A. \tag{21}$$

We are interested in finding air density ρ. Given are the reference area A (often defined as the largest cross-sectional area of the vehicle [59]) and the mass of the vehicle. The velocity V_a is the magnitude of the wind-relative velocity, $V_a \equiv \left\|\mathbf{V}_{\text{inert}} - \mathbf{V}_{\text{wind,bulk}}\right\|$, where $\mathbf{V}_{\text{inert}}$ is the inertial velocity and $\mathbf{V}_{\text{wind,bulk}}$ the atmospheric bulk velocity, and C_A is the axial aerodynamic force coefficient, which is a function of the wind-relative orientation and flow environment of the craft.

As a first approximation, we may assume the HFV to be aligned with the wind vector, taking the angles of attack and sideslip to be $\alpha = \beta = 0$, thereby making C_A only a function of the flow conditions. If we only consider the upper strata of the atmosphere, where rarefied flow is in effect, we may approximate the coefficient of axial force by means of

classical Newtonian theory, which yields $C_A \approx 2$ for a blunt body [72]. From Newtonian theory, a flat plate in rarefied crossflow will have an axial drag coefficient of 2, and is traditionally taken as a first approximation in preliminary aerodynamic design [72]. Withers et al. [59] have remarked that this forms an excellent approximation for many entry vehicles, and our own simulations have supported this claim as presented later. Now, it is possible to approximate ρ as

$$\rho \approx -\frac{m}{AV_a^2} a_x. \tag{22}$$

3. Atmosphere in the continuum flow regime

Given the fact that Newtonian theory only holds in a fully rarefied flow regime (i.e., Knudsen number $\mathrm{Kn} \geq 2\times10^{-2}$), the above model's validity is short lived; as the vehicle passes the upper layers of the atmosphere, greater discrepancies are found, since the axial drag coefficient starts to decrease as the flow starts to transition to a continuum flow [47]. Therefore, an alternative relation is needed. Following the treatment in [73, pp. 2-1–2-2], we consider the buoyancy equation:

$$\frac{\mathrm{d}p}{\mathrm{d}h} = -\rho g, \tag{23}$$

where p is the pressure and h is the altitude. From the equation of state, we may define a *scale height* $H \equiv RT/g$, where T is the temperature and R is the specific gas constant, and g is the gravitational acceleration. If we assume the atmosphere to be isothermal, we may find the rate of change of pressure with time to be [33]:

$$\dot{p} = \frac{\mathrm{d}p}{\mathrm{d}t} = -\rho g \frac{\mathrm{d}h}{\mathrm{d}t} = -\rho g V_r, \tag{24}$$

where V_r is the radial component of velocity in the local (instantaneous) radial coordinate frame; we have assumed density to be approximately constant. In order to find the time rate of change of density, we will need the equation of state of an ideal gas [71]:

$$p = \rho RT. \tag{25}$$

Then, it follows that the time rate of change of density will be approximately equal to [30]:

$$\dot{\rho} = \frac{\mathrm{d}\rho}{\mathrm{d}t} = \frac{\mathrm{d}p}{\mathrm{d}t}\frac{\mathrm{d}\rho}{\mathrm{d}p} = \frac{\mathrm{d}p}{\mathrm{d}t}\frac{1}{RT} = -\rho g V_r \frac{\rho}{p} = -\frac{\rho^2 g V_r}{p}. \tag{26}$$

4. Applicability of the atmospheric models

We now consider the transition between the two flow regimes so as to determine which model to use. For a Mars and Earth atmosphere, any altitude above about 7.5 scale heights can be considered to be rarefied, and Newtonian theory forms an adequate approximation [73, 74]. For Earth, this translates to around 60 kilometers in altitude, while on Mars this is around 80 kilometers. As such, we propose to employ the acceleration-based formulation for altitudes above this threshold, allowing for adequate density estimates to be obtained. With these estimates, it is then possible to propagate the density and pressure profile through the above rate of change equations by means of numerical integration and knowledge of the inertial velocity. There remains, however, one problem: a datum for pressure has not been given. Withers et al. [59] propose to utilize the hydrostatic equation to produce an estimate for the pressure at the start of the density profile ($r = r_0$), yielding the following approximate relation:

$$p(r_0) = \rho(r_0) g(r_0) \left(\frac{\mathrm{d}(\ln\rho)}{\mathrm{d}r}\Big|_{r_0} \right)^{-1}. \tag{27}$$

Considering the fact that we cannot afford to assume the pressure to be zero, since this will produce a singularity in Eq. (26), we can use Eq. (27) to produce the integration constant needed to propagate the pressure, since fluctuations in a_x cause significant changes in ρ when obtained using Eq. (22). The derivative found in the function above can be very sensitive to noise. Therefore, we propose an alternative method that assumes prior knowledge of the atmospheric scale height H:

$$p(r_0) \approx \rho(r_0) g(r_0) H. \tag{28}$$

In practice, the scale height is almost always known [73]. With this knowledge, we propose to reconstruct the atmosphere in real-time, adhering to the following procedure:

Step 1) Filter the axial accelerations using CCMLE.
Step 2) Compute the approximate density from the inertial velocity and filtered angular acceleration, assuming $C_A \approx 2$ (see Eq. (22)).
Step 3) From the density, compute a datum pressure value using Eq. (28).
Step 4) Propagate the pressure by integrating the value from Eq. (24), and keep computing the density using Eq. (22).
Step 5) Below some specified altitude below which the rarefied flow assumptions fail to hold (e.g., $h \leq 7.5H$), propagate the density by integrating the result from Eq. (26).

Having predicted the vehicle's attitude, as well as the atmospheric conditions it experiences, we now wish to obtain predictions of the atmospheric conditions. These predictions will be updated as more data become available through filtering, and will allow for the current atmospheric conditions to be known even when the filter is still accumulating the current n samples. The next section presents a general formulation that allows any time series to be predicted m-steps ahead in time.

IV. Near-Term Prediction

As mentioned previously, there is an appreciable delay between the accumulation of a sample window, the time it requires to filter the data, and the population of the next window. Consider a sampling rate of $f_{\text{sample}} = 200$ Hz, which is representative of modern inertial measurement units [39, 44, 45, 59]. In this case, considering a window size of 100 elements, we would have to wait 500 milliseconds for samples to accumulate. A larger window size, or a windowless approach where all previous data are analyzed in one optimization problem given by Eq. (6), not only increases the time that is required to sample it, but also increases computational complexity significantly [54]. Withers and Catling [39] duly note that such time scales are well below those of atmospheric processes, allowing us to employ a linear prediction scheme to determine near-term atmospheric properties as the CCMLE algorithm is running. These quantities could be used in model predictive control, as is frequently done in terrestrial applications [75, 76]. Given the short time frames and the assumed stochastic stationarity of the processes, we propose the use of a linear discrete-time time-invariant autoregressive (AR) model [77–80].

The general the general structure of an autoregressive system is denoted as follows [77, 80]:

$$y(k) + a_1 y(k-1) + a_2 y(k-2) + \ldots + a_{n_a} y(k-n_a) = \xi(k), \tag{29}$$

where $\{y(k)\}$ and $\{u(k)\}$ are the system output and input signals, respectively, with $k \in \mathbb{Z}^+$. $\xi(k)$ is a noise sequence, which is assumed to be i.i.d. with zero mean and finite variance. The polynomial order is denoted by a nonnegative integer $n_a \in \mathbb{Z}^+$.

A. Parameter identification

We will now proceed with what is known as *system identification* or *parameter identification*, in which we aim at finding an estimate of the $\{a_i\}_{i=1}^{n_a}$ values using past values of $y(k)$. These values of $y(k)$ are derived from the filtered CCMLE time series as described in the previous section. Since we cannot observe the noise signal $\xi(k)$ directly, and only have observations of y up to time k at our disposal, we must identify the parameters only using these past observations. For this task, we consider the recursive least squares (RLS) estimator as presented by Ljung and Söderström [77]. If the true process is linear and of the same or lower order as the model, the model will produce maximum likelihood estimates of y, provided the noise process $\xi(k)$ is i.i.d. and is sampled from a zero mean normal distribution [77]. Let us define parameter vector $\boldsymbol{\theta}$ of the form:

$$\boldsymbol{\theta} = \begin{bmatrix} a_1 \\ a_2 \\ \vdots \\ a_{n_a} \end{bmatrix} \tag{30}$$

given the vector of lagged output data $\boldsymbol{\varphi}(k)$:

$$\boldsymbol{\varphi}(k) = \begin{bmatrix} -y(k-1) \\ -y(k-2) \\ \vdots \\ -y(k-n_a) \end{bmatrix} \tag{31}$$

Now, we find the following recursive algorithm based on an offline least squares method to estimate unknown parameters $\boldsymbol{\theta}$, giving parameter estimate $\hat{\boldsymbol{\theta}}$:

Algorithm 1 Recursive Least Squares Parameter Estimator

$\hat{\boldsymbol{\theta}}(0) \leftarrow \mathbf{0}_{n_a}$
$\boldsymbol{\varphi}(0) \leftarrow \mathbf{0}_{n_a}$
$\mathbf{P}(0) \leftarrow C\mathbf{I}_{n_a \times n_a}$
$k \leftarrow n$

while $k < (N+1) \cdot n$ **do**
  $\mathbf{L}(k) \leftarrow \frac{\mathbf{P}(k-n)\boldsymbol{\varphi}(k)}{1/\lambda + \boldsymbol{\varphi}^{\mathsf{T}}(k)\mathbf{P}(k-n)\boldsymbol{\varphi}(k)}$
  $\mathbf{P}(k) \leftarrow \mathbf{P}(k-n) - \mathbf{L}(k)\boldsymbol{\varphi}^{\mathsf{T}}(k)\mathbf{P}(k-n)$
  $\hat{\boldsymbol{\theta}}(k) = \hat{\boldsymbol{\theta}}(k-n) + \mathbf{L}(k)\left[y(k) - \hat{\boldsymbol{\theta}}^{\mathsf{T}}(k-n)\boldsymbol{\varphi}(k)\right]$
  Wait for new window.
  $\boldsymbol{\varphi}(k+n) \leftarrow [-y(k+n)\ -y(k-1+n)\ \cdots\ -y(k-n_a+n)]^{\mathsf{T}}$
  $k \leftarrow k+n$
end while

The above algorithm solves the least squares problem for $\boldsymbol{\theta}$ that satisfies the following minimization [77]:

$$\boldsymbol{\theta}^* = \arg\min_{\boldsymbol{\theta}} \frac{1}{n} \sum_{k=1}^{n} \lambda \left[\mathbf{y}(k) - \boldsymbol{\theta}^{\mathsf{T}}\boldsymbol{\varphi}(k)\right]. \tag{32}$$

This minimization is done in a recursive manner in the above algorithm (details on which can be found in, e.g. [77]), and allows more values to be included in the parameter identification process as they become available. Since it can be shown that for $\mathbf{P}^{-1}(0) \to \mathbf{0}$, the recursive estimate approaches the offline estimate (which solves the minimization problem with no errors), C is taken to be a large constant to approximate this criterion, as per the guidelines of Ljung and Söderström [77]. λ is the forgetting factor, which when decreased, gives greater weight to recent samples, allowing for faster adaptation but also more fluctuation. In practice, it is taken between 0.98 and 1 [81]. In our case, C is taken as 10^6, and $\lambda = 1$. Naturally, we must stipulate $n_a < n$, so as to ensure it can be calculated using the past window of values. In addition, here we have taken each window to be n samples long, and there to be N windows in total; we take the last n_a samples of the last window to use in the algorithm.

The above algorithm only performs one-step-ahead predictions. Let us assume we wish to perform an m-step-ahead prediction. We may readily find the following result by performing successive substitution, yielding what is known as multi-step-ahead predictive identification (MSPI) [82]:

$$\begin{aligned}
\hat{y}(k+1|k) &= \theta_1^{(1)} y(k) + \ldots + \theta_{n_a}^{(1)} y(k-n_a+1) \\
\hat{y}(k+2|k) &\approx \left[\theta_1^{(1)}\theta_1^{(1)} + \theta_2^{(1)}\right] y(k) + \theta_1^{(1)}\theta_2^{(1)} y(k-1) + \ldots \\
&= \theta_1^{(2)} y(k) + \theta_2^{(2)} y(k-1) + \ldots + \theta_{n_a}^{(2)} y(k-n_a+1) \\
\hat{y}(k+3|k) &= \theta_1^{(3)} y(k) + \theta_2^{(3)} y(k-1) + \ldots + \theta_{n_a}^{(3)} y(k-n_a+1) \\
&\vdots \\
\hat{y}(k+m|k) &= \sum_{i=1}^{n_a} \theta_i^{(N)} y(k-i+1)
\end{aligned} \tag{33}$$

To 'train' the parameter vector using the RLS estimator, we must shift the above result back by m samples, yielding:

$$\hat{y}(k|k-m) = \sum_{i=1}^{n_a} \theta_i y(k-i+1-m) \tag{34}$$

Therefore, in above algorithm, we simply replace the $\boldsymbol{\varphi}(k+n)$ step (Ln. 11) by:

$$\boldsymbol{\varphi}(k+n) \leftarrow \begin{bmatrix} -y(k+n-m) & -y(k-1+n-m) & \cdots & -y(k-n_a+n-m) \end{bmatrix}^{\mathsf{T}}. \tag{35}$$

This will give us a parameter vector $\boldsymbol{\theta}$ that will provide us with an m-step-ahead prediction. Since the number of past values that we need access to increases quickly for increased n_a and prediction window m, it is best to keep this as low as possible, such that the matrix algebra that is to be performed on-board is kept simple and storage requirements are kept low. Keeping n_a reasonably high is advisable, as more of the process dynamics will be captured that way; as a matter of fact, as $n_a \to \infty$, all processes can be captured by the autoregressive model [83]. Note that this asymptotic convergence limit does not tell anything about the rate of convergence, and it should not be taken as an incentive to increase n_a to higher than necessary values; in practice, it becomes apparent when an increase in n_a stops yielding increased performance (see e.g., [84]). In operational practice, it becomes necessary to apply this estimation methodology at a decreased sampling rate, so as to keep the computational effort in check; this will yield a smaller number of predictors to be updated, thereby allowing for timely delivery of predictions at an acceptable frequency.

V. Application to the Mars Phoenix Lander

The Mars Phoenix lander landed on May 28th, 2008 on the Martian North Pole [63]. The Phoenix entry vehicle is a 70 degree sphere cone shaped capsule with a diameter of 2.65 m and an entry mass of 572.743 kilograms [39]. During the hypersonic entry phase, the vehicle was unguided and not spin stabilized, following a purely ballistic trajectory [63]. After peak heating and peak deceleration, the vehicle slowed down to a Mach number of 1.65, when the supersonic disk-gap-band parachute was deployed, followed by the terminal landing phase [63]. The complete EDL sequence from entry interface to touch down took approximately 420 seconds, while the ballistic phase lasted approximately 230 seconds [39]. The relative timing and main events during the EDL sequence are shown in Fig. 2.

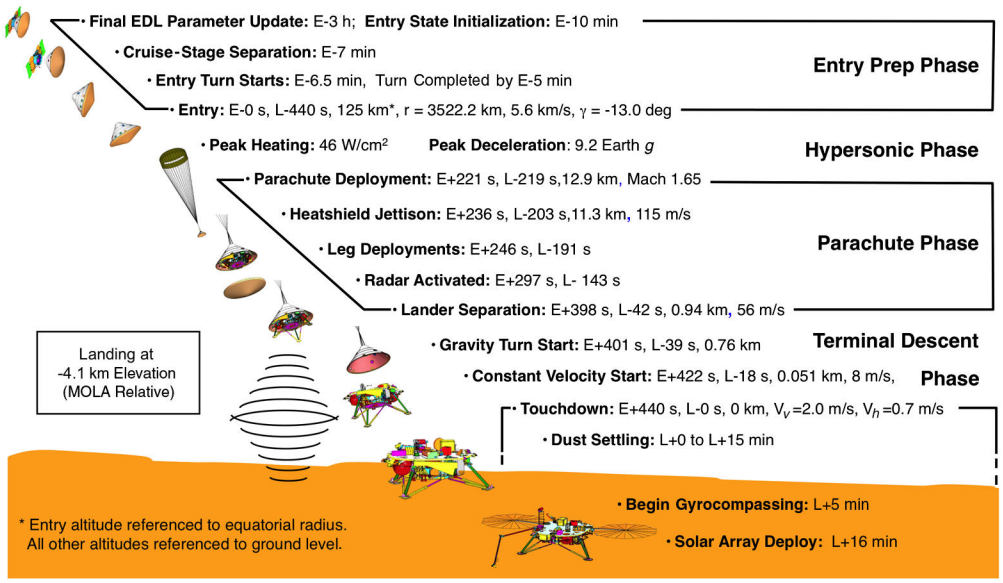

Fig. 2 Mars Phoenix nominal EDL sequence [63]

In the following subsections, we aim to reconstruct the atmospheric properties encountered by the vehicle during the hypersonic phase of its entry. To accomplish this objective, we first consider the inertial entry state of the Mars Phoenix lander as found in [40]. To propagate this state, we apply CCMLE filtering to the IMU data, so as to reduce its noise after which we can apply those filtered measurements to reconstruct the trajectory from the entry interface onwards.

Having reconstructed the trajectory, we utilize the inertial velocity to estimate the atmospheric profile. Then, the vehicle attitude is determined from the filtered gyroscope measurements and inertial velocity vector, for comparison to other data. Using these results, we finally demonstrate the performance of our autoregressive model when applied to density and pressure prediction.

A. Entry state

The Phoenix entry state is obtained from an *a priori* onboard orbit determination solution known as OD77, which utilized a previous star tracking attitude and propagates the state using inertial measurements [40]. We remark that the OD77 epoch is delayed by 68 ms with respect to the pre-defined entry interface epoch at a radial distance of 3522 km from the center of mass of Mars [39, 40]. This state is shown in Tab. 1 in the Earth Mean Equator of January 2000 (EMEJ2000) inertial frame centered on Mars:

Table 1 Mars Phoenix OD77 EMEJ2000 initial conditions [40]

Parameter	Value
X (m)	1060304.16809705
Y (m)	-645136.486623493
Z (m)	3296270.9865079
$\dot{X}$ (m/s)	1464.27469596023
$\dot{Y}$ (m/s)	5350.16886003297
$\dot{Z}$ (m/s)	-770.68622121074
t_0 (UTC)	2008-05-25T23:30:57.801

Since our primary interest is not in the absolute position of the vehicle in a Mars-relative frame, we shall carry out our calculations in the EMEJ2000. For convenience, we have listed the initial rotation matrix to the Mars-Centered Mars-Fixed (MCMF) frame at t_0, and to the Phoenix cruise frame ('C frame', or CF) at the entry interface are derived from the quaternions (based on the JPL quaternion convention) as stated in [40]:

$$\mathbf{R}^{\text{MCMF}}_{\text{EMEJ2000}} = \begin{bmatrix} -6.55644577 \times 10^{-1} & 7.55069658 \times 10^{-1} & 2.24550277 \times 10^{-6} \\ -7.55069653 \times 10^{-1} & -6.55644572 \times 10^{-1} & -1.20245955 \times 10^{-4} \\ -8.93218207 \times 10^{-5} & -8.05341195 \times 10^{-5} & 9.99999993 \times 10^{-1} \end{bmatrix} \tag{36}$$

$$\mathbf{R}^{\text{CF}}_{\text{EMEJ2000}} = \begin{bmatrix} 0.25649721 & 0.35289633 & 0.89981852 \\ 0.95982388 & 0.01659863 & -0.28011176 \\ -0.11378616 & 0.93551519 & -0.33446082 \end{bmatrix} \tag{37}$$

The relative orientation of the trajectory is shown in Fig. 3 in the MCMF frame.

Fig. 3 Entry trajectory geometry in a Mars centered Mars fixed frame

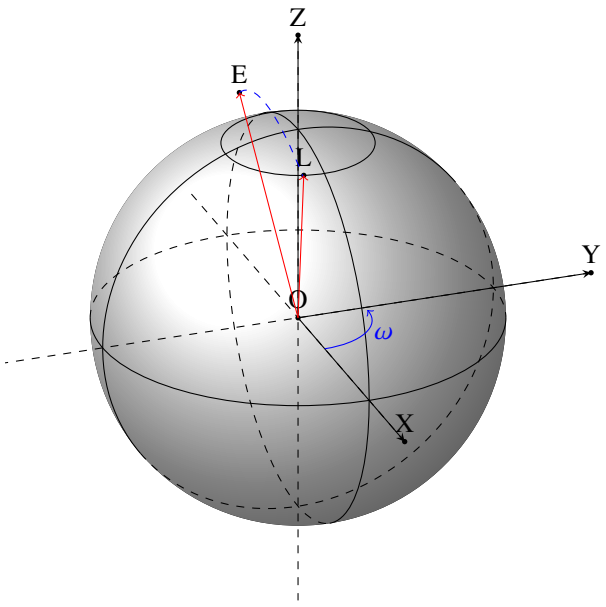

B. Signal noise reduction

We shall employ the CCMLE algorithm on the IMU sensor signals with a fixed window length of $n = 100$ samples, making for a total of 45500 samples or $N = 455$, which is equivalent to a time frame of $\Delta t = 227.5$ s from the entry interface to approximately parachute deployment [40]. The CCMLE algorithm is implemented in its windowed form with an initial equality constraint, and is modified to take a single value of ε per signal that is applied as a universal constraint to that particular signal. Tab. 2 lists all the gradient bounds $\underline{\varepsilon} \equiv \varepsilon/h$, where $h = 5$ ms is the sampling period, as used in this work:

Table 2 Gradient bounds applied to CCMLE filtering for the Mars Phoenix entry data

Parameter	**Gradient bound $\underline{\varepsilon}$**	**Unit**
$a_{x,\text{body}}$, x_{body} (axial) acceleration	3.0	m s^{-3}
$a_{y,\text{body}}$, y_{body} (normal) acceleration	0.08	m s^{-3}
$a_{z,\text{body}}$, z_{body} (normal) acceleration	0.08	m s^{-3}
Ω_x, x_{body} angular velocity	0.02	rad s^{-2}
Ω_y, y_{body} angular velocity	0.08	rad s^{-2}
Ω_z, z_{body} angular velocity	0.08	rad s^{-2}

Relating back to our previous discussion, the above gradient bounds are equal to bounds on the maximum jerk and angular acceleration that is expected to occur; this forms an intuitive means of tuning the CCMLE filter, and is firmly grounded in physical reality. In this case, the above values were determined by considering the filtered data from Withers and Catling [39] and the relative magnitudes of the numerically computed gradients between the filtered data (from [39]) and raw data.

Filtering the data is very straightforward thanks to the conciseness of the C interface produced by CVXGEN. Fig. 4 shows the raw data (EDR, for 'experimental data records') in blue, with both the CCMLE results and the Withers and Catling [39] (W&C) results to demonstrated the adequacy of the filtering results. The results by Withers and Catling [39] were produced with full knowledge of the approximate vehicle aerodynamics and final landing location, and serve

as a nominal guideline to which we compare our results. Note that body angles were provided as quaternions by Withers and Catling [39], which would have introduced additional noise had we differentiated them with respect to time; these rates are therefore omitted, but can be ascertained in the work of Karlgaard and Tynis [40].

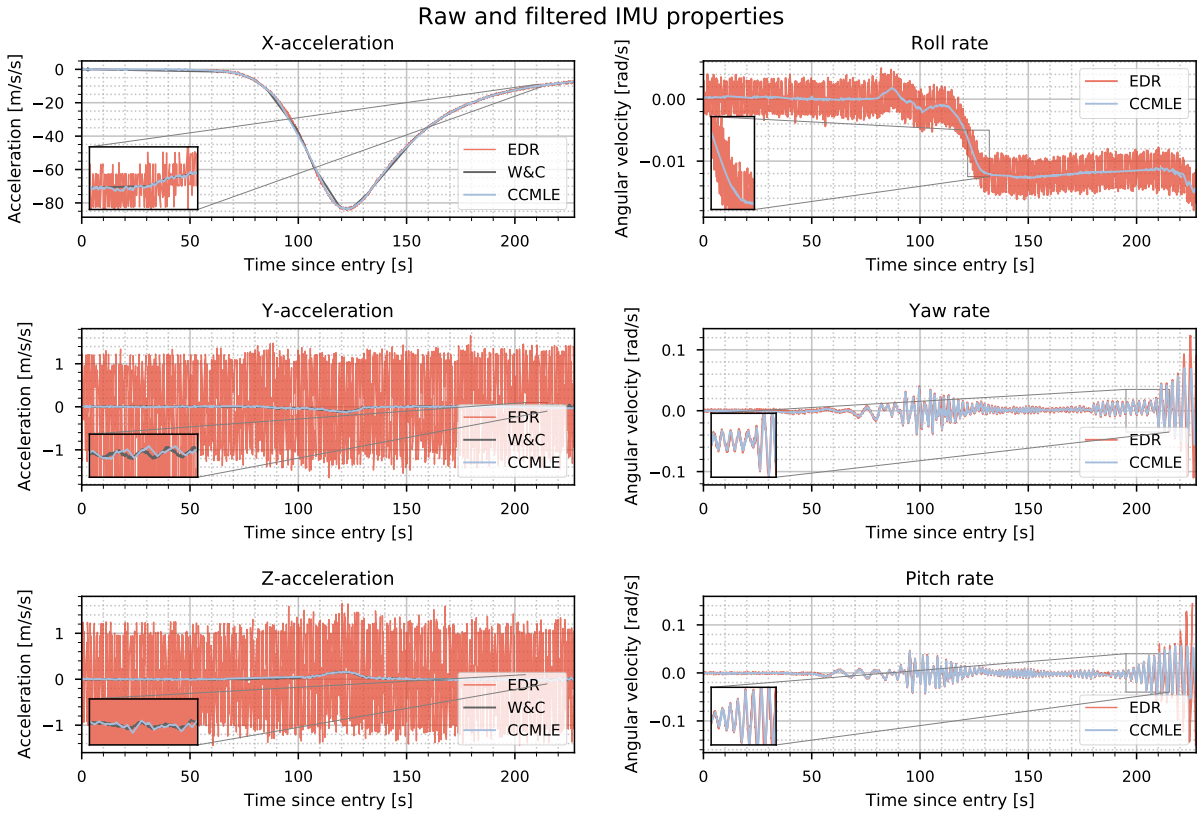

Fig. 4 Raw and filtered inertial measurement properties for the Mars Phoenix lander

In an effort to determine the accuracy of our filter in an online setting, in which the number of numerical operations is to be limited, we have performed a simple Riemann sum-based integration on the computed inertial accelerations, as per the above derivations. This has produced rather satisfactory results (see Fig. 5), with a maximum velocity error of $5.8\,\mathrm{m\,s^{-1}}$ and a maximum radius error of 4.2 km, near parachute deployment; this likely stems from the numerical error that propagates from residual noise and the numerical integration scheme. In addition, we must note that Withers and Catling [39] applied forward and backward estimates (from the *a posteriori* landing location), which are subsequently combined using a modified Bryson–Frazier smoother [30, 85]. Since our goal is not to determine the absolute vehicle position, errors in the position are of no great concern.

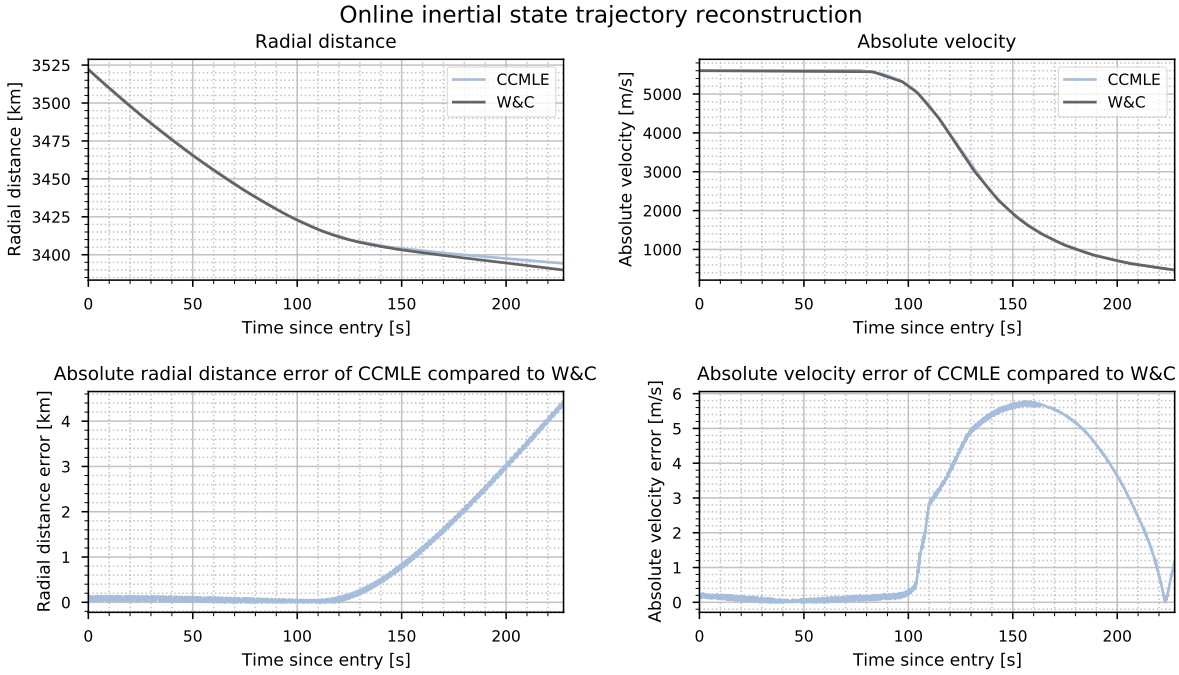

Fig. 5 Inertial state trajectory reconstruction results

Considering the above results, we find that the results from Withers and Catling [39] closely match those produced using CCMLE, especially when considering the velocity estimate which will extensively use in the following subsections. While CCMLE takes intuitive rate of change bounds as its input, the approach of Withers and Catling [39] relies on a combination of moving-average windows of different, heuristically determined, lengths. In addition, both forward and backward integration were applied from the entry state and the landing site, respectively. The approach of Withers and Catling [39] thus requires *a posteriori* knowledge that our algorithm does not. Most importantly, the procedure of Withers and Catling [39] is heavily reliant on the use of an aerodynamic database. Our approach requires only knowledge of the rate of change bounds, and uses only past values in its implementation, making it suitable for online use, in which it can directly generate atmospheric estimates, as shown in the next subsections.

C. Atmosphere reconstruction

We shall first consider the estimation of the density field in the rarefied flow regime. Since it is more convenient to work with a time window as opposed to some boundary altitude, we have chosen to consider the atmosphere encountered during the first 50 s since reentry to be (close to) rarefied; this checks out given the altitude requirements discussed previously. To obtain immediate results, we utilize the inertial velocity approximation for the relative velocity. In addition, to find a datum for the pressure near the entry interface, we shall employ Eq. (28), given a scale height of $H = 11.1$ km [86]. In addition, the rate of change equations for both properties are evaluated to show that this constitutes an adequate bootstrapping method. The results are shown in Fig. 6:

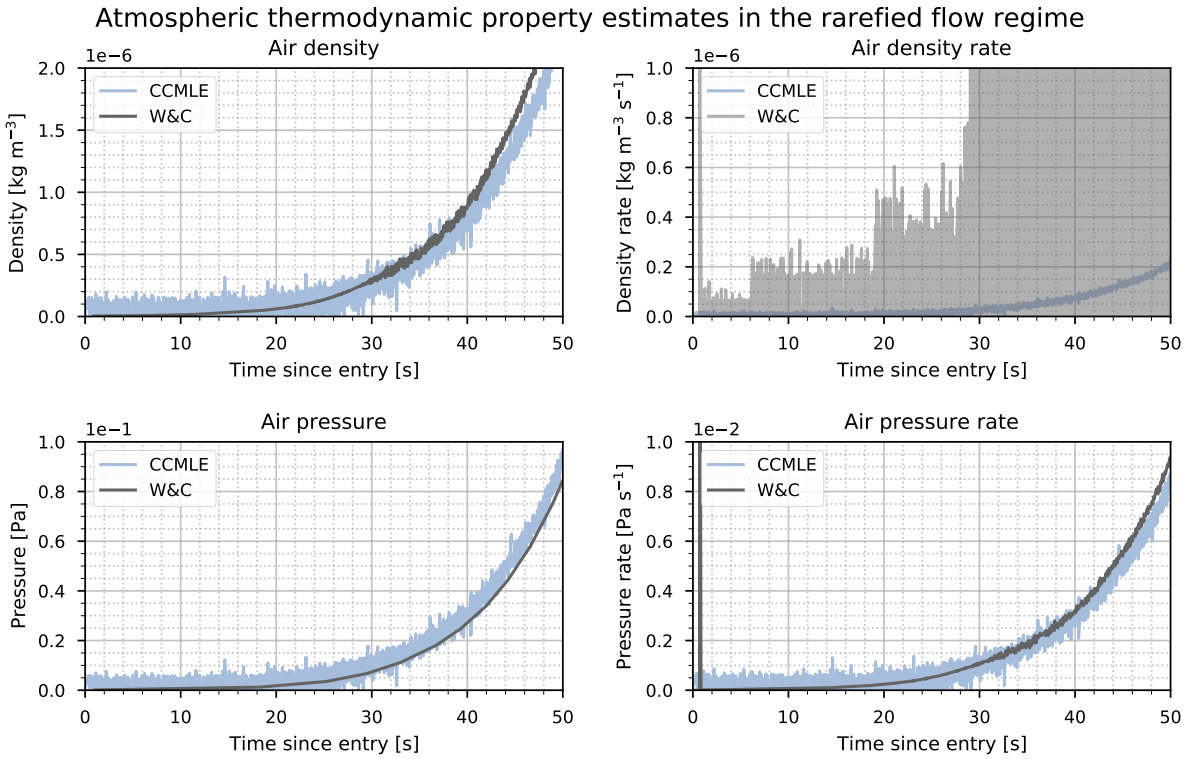

Fig. 6 Rarefied atmosphere thermodynamic property reconstruction results

Overall, we observe that adequate results are obtained in the higher atmospheric layers earlier on in the EDL phase. Of particular interest are is the air density rate, which is much more stable in the case of CCMLE, when compared to the values from [39]. This is attributed to the fact that the underlying IMU measurements have been limited in their rate of change when they were filtered using CCMLE, and this bound still persists after Eq. (26) is evaluated. The type of smooth behavior observed in the rate of change of air density in the CCMLE case is characteristic of air density shear in actual atmospheres, and is therefore more realistic [41, 73].

The air density and pressure estimates obtained in the rarefied flow regime can readily be used to propagate the time derivatives obtained previously. Here, we take the maximum of the estimated density and pressure over the first 15 s since entry, and take those to be the values at $t - t_0 = 15$ s, from which we propagate them. The reason for this time stems from the fact that the vehicle reaches an altitude of 80 km near that time. An altitude of 80 km is around the limit of the rarefied flow assumption, as discussed earlier. In practice, it was seen that a correction factor is needed for the density at the epoch, since the $C_A \approx 2$ assumption starts to lose validity for such a window length; conversely, limiting the period over which the rarefied assumptions are taken true will produce an initial estimate that is extremely susceptible to noise and will amplify errors, as it appears in the denominator of the rate of change. We have therefore chosen to implement a correction factor of 1.05, which roughly corresponds to the density estimate (see Eq. (22)) correction ratio of $2/C_A$, for $C_A \approx 1.9$, and approximately holds for the Phoenix Lander over this regime [39]. This implies that at least some rudimentary knowledge of the static aerodynamics of the vehicle is needed, but is only limited to the axial drag coefficient in the rarefied regime.

Given this correction, we find our approach to closely match the results from both [59] and a simulated profile from the Mars Global Reference Atmospheric Model 2010 (Mars-GRAM 2010, [41]). This supports the use of our approach and underlines the necessity of an axial drag coefficient estimate. Given this correction factor, we find the following density and pressure fields over the complete hypersonic regime (Fig. 7):

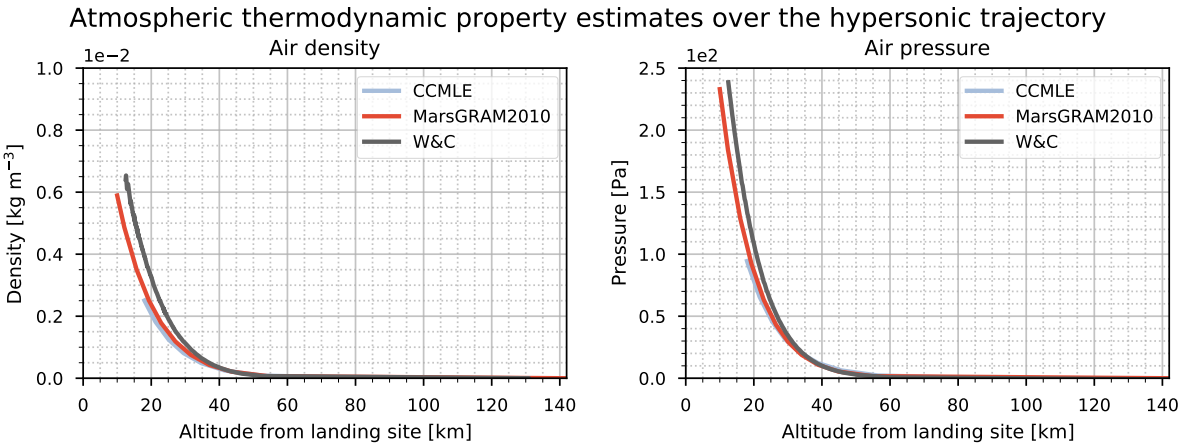

Fig. 7 Hypersonic regime atmosphere thermodynamic property reconstruction results

Note that these air density and pressure estimates may be indefinitely propagated, provided that the estimates of the radial velocity and position are available. As a first approximation, sufficiently accurate results can be obtained by assuming a constant gravity field, thereby requiring only predictions of the radial velocity. This assumption enables us to compute short-term predictions of the air density and pressure the vehicle will encounter as it continues on its trajectory, knowledge of which can be supplied to a guidance algorithm in the case of an actively controlled vehicle [6]. We shall shortly show how these air density and pressure predictions can be obtained by applying the parameter identification routine presented before.

D. Wind-relative attitude reconstruction

We shall first consider the angle of attack, an estimate for which is presented by Withers and Catling [39]. Using the previously identified relations, given the current velocity vector and body Euler angles, we can find our scheme to yield an angle of attack estimate as shown in Fig. 8:

Fig. 8 Angle of attack estimate in the hypersonic regime

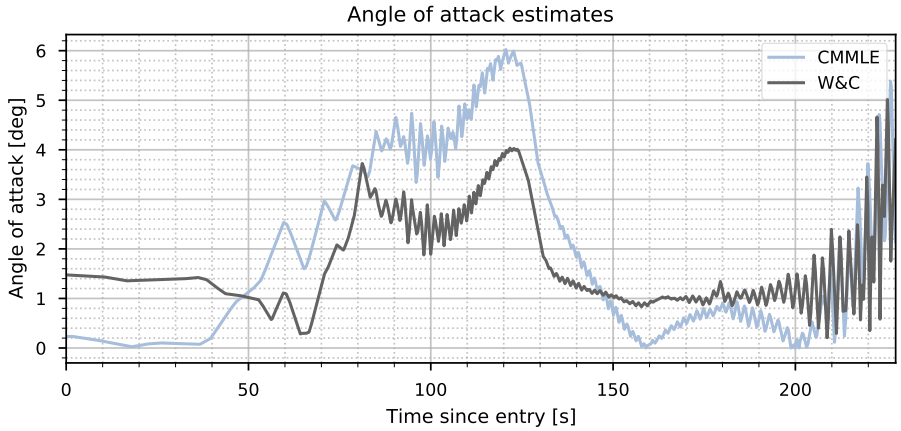

As can be observed, a bias of roughly two degrees is found between 70 and 130 s. Both Withers and Catling [39] and Karlgaard and Tynis [40] have observed a similar but smaller discrepancy when using the IMU measurements and an *a priori* aerodynamic database; there results, however, agree mutually despite using different reconstruction techniques, so we assume both of their results to be correct. Desai et al. [63] have noted that this slight discrepancy in the case of [39, 40] stems from a minor malalignment of the heatshield, but in our case we believe it to be an artifact of

the rather inaccurate (yet efficient) integration scheme employed to propagate the body attitude, as well as compute the velocity vector. Regardless, general trends can clearly be identified.

E. Atmospheric prediction

As discussed previously (Sec. IV), we shall employ an m-step-ahead autoregressive predictor to determine future values of the air density. We predict $m = 1000$ steps ahead, which is equivalent to 5 seconds in the future. We have taken our polynomial size to be $n_a = 10$, and updated the RLS algorithm every $n = 100$ samples. The results are shown in Fig. 9:

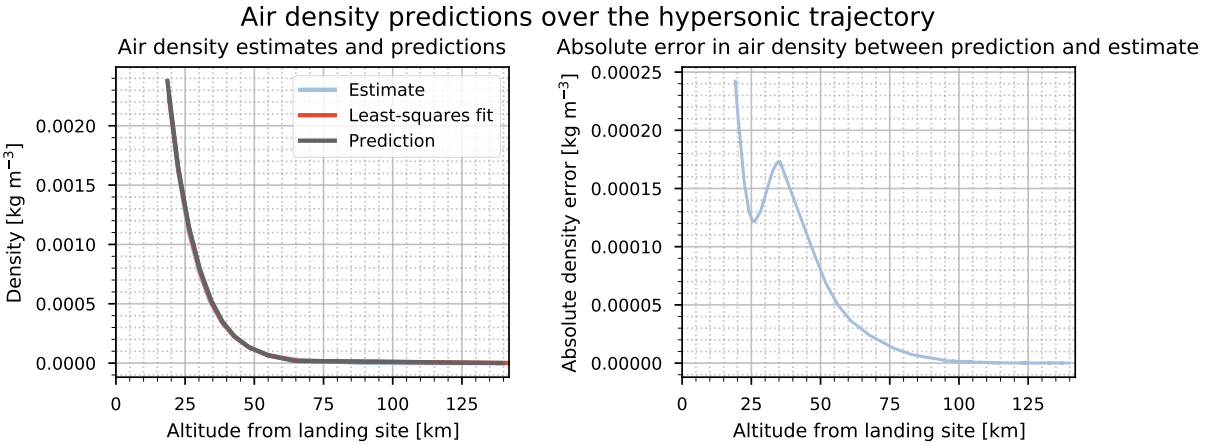

Fig. 9 Hypersonic regime atmospheric density prediction results

Here, the estimates correspond to those values of air density that have been computed with knowledge up to their time i.e., $\hat{\rho}(k|k)$. The predictions are m-step-ahead predictions of the estimates, determined using data that are obtained m-steps-ahead of the predicted point in time i.e., $\hat{\rho}(k|k-m)$. Finally, the least-squares fit shows the values of $\hat{\boldsymbol{\theta}}^{\mathsf{T}}(k)\boldsymbol{\varphi}(k)$, which are approximately equal to $\hat{\rho}(k|k)$ in a least-squares sense.

As can be seen, even for such large time step as 0.5 s, the prediction errors are low enough to be useful for use in predictive guidance schemes. Since the time scales we have considered here are well below those of the atmospheric processes [39], errors have remained low even at a small polynomial order. Incidentally, an increase in polynomial order did not yield any accuracy improvements.

VI. Conclusion

In this work, we have presented a novel approach to online filtering of IMU measurements, known as CCMLE. This approach forgoes many of the limitations of the extended Kalman filters, in that it does not require the computation or estimation of a Jacobian matrix, nor the solution of a (set of) Riccati equation(s). As the CCMLE solution procedure involves the solution of a convex quadratic programming problem, it can be efficiently solved on modest hardware using specially tailored embedded solvers such as CVXGEN. As for using the CCMLE filter, we have shown that the bound vector $\boldsymbol{\varepsilon}$ can be determined from preliminary engineering simulations or design specifications, and can be adjusted intuitively by relating it to signal error statistics.

As a preliminary exposition of the capabilities of the CCMLE filter, we have presented its application in the framework of a HFV navigation system during atmospheric entry. We have presented a general approach to data reduction, which forms the basis of enabling an unbiased approach to obtaining the present vehicle state, attitude, and local atmospheric properties. We have presented a simplified approach that relies almost exclusively on matrix-vector operations, and can readily be applied on an HFV, provided an initial (entry) state is available. From this state, all the above parameters can be estimated using the CCMLE-filtered IMU readings. To enable a continuous stream of data to be secured, as well as to obtain near-term predictions, a simple autoregressive model is presented and implemented using recursive least-squares. Using this approach, no vehicle properties are needed to be known at the time of entry, except for the vehicle's initial mass and area. By assuming the vehicle to be tangent to the wind vector, and assuming it

to be blunt body in the rarefied flow limit during the first stages of entry, we can obtained a primer on the density and pressure. Beyond this assumption in the rarefied flow regime, none of the vehicle dynamics are assumed.

To demonstrate the aforementioned theory, we have turned to the Mars Phoenix lander and have analyzed its trajectory from the entry interface up to parachute deployment. The CCMLE estimates of the IMU data closely match those produced through previous data reduction efforts that assume vehicle properties [39, 40], and produce adequate inertial trajectories when integrated using a simple trapezoidal scheme. Since we have shown that stationary Gaussian processes get filtered out completely using our method, we believe CCMLE produces more reliable results when applied to highly noisy data, since no errors originating from erroneous vehicle dynamics are introduced, which would have been the case when using Kalman filter schemes. From this filtered data, two thermodynamic parameters of the atmosphere, namely density and pressure, were retrieved as derived from first principles. While the assumption of an axial force coefficient of 2 produced poor results, but a simple change to a more realistic value of 1.9 greatly improved the performance of our algorithms, closely matching results from the Mars-GRAM 2010 model. This gives cause to the conclusion that Newtonian theory will not produce adequate atmospheric profiles, and proper knowledge of the static aerodynamic properties of a vehicle in the rarefied regime are needed to achieve correct atmospheric estimates. In future work, it would be desirable to quantify the effect of an erroneous initial estimate of the static vehicle dynamics on the atmosphere profile produced, and the importance of a correct initial axial drag coefficient. As of yet, the authors have found no way to remove any assumed model of the static aerodynamics, which would inadvertently introduce model errors that quickly propagate through the rest of the atmospheric profile. If an initial density would be assumed, errors in its value would propagate through the resulting profile and could greatly alter its shape (see Eq. (24), in which density appears in the denominator). Future efforts may focus on quantifying the effect of an arbitrary or modeled first density estimate.

Following the atmospheric reconstruction phase, we have taken to reconstructing the aerodynamic angles of the entry vehicle. These results showed similar trends as previous construction efforts, but showed a consistent shift of around two degrees for a great portion of the trajectory. This is currently attributed to the low order of accuracy of the integration scheme employed, of where the errors have likely corrupted the inertial state and attitude estimates of the vehicle. Refining this scheme at the cost of slightly increased computational effort should alleviate this problem.

Finally, prediction results for the air density profile have been demonstrated, and good performance and accuracy were found for a large prediction window and a small polynomial order. These results suggest that autoregressive models of low order produce good estimates even when used a significant number of steps in the case of a high sampling rate. As has been discussed before, this is only possible because the time scales of atmospheric processes during entry are greater than those of the prediction window, therefore allowing for those atmospheric processes to be approximated as stochastically stationary linear processes between predictions. The existence of an underlying stochastically stationary linear processes makes time series such as the density profile amenable to prediction using autoregressive models.

In future work, the CCMLE filter will be studied in greater depth to find properties regarding its learning rate. By learning rate we refer to the number of samples required before estimates are obtained within a certain error bound, given any initial estimate within certain bounds from the true initial state. This will allow us to determine the minimal window size necessary to estimate the dynamics of the system within a particular error bound, and achieve a correct estimate at a certain confidence within a given number of samples depending on the noise properties of the signal. In addition, the effect of erroneous initial estimates, such those introduced by an erroneous initial state, will be studied to determine the robustness of CCMLE to such samples. Beyond these topics, the effect of outliers and biased or offset data will be explored. All of these efforts will result in a model of the worst case performance of CCMLE, allowing errors to be bound and heuristics to be obtained to ensure a minimum level of accuracy. These results can then be applied to similar problems in guidance and navigation of HFVs, ultimately allowing not only for measures of learning rate to be known beforehand, but also for change detection and bias correction that would be advantageous in when applied in rapidly changing environment such as those encountered in hypersonic flight.

References

[1] Dechant, L. J., "Effect of Freestream Velocity Disturbances on Hypersonic Vehicles," *Journal of Spacecraft and Rockets*, Vol. 49, No. 4, 2012, pp. 751–756. doi:10.2514/1.A32113.

[2] Hale, N., Lamotte, N., and Garner, T., "Operational Experience with Hypersonic Entry of the Space Shuttle," *AIAA/AAAF 11th International Space Planes and Hypersonic Systems and Technologies Conference*, American Institute of Aeronautics and Astronautics, Orleans, France, 2002. doi:10.2514/6.2002-5259.

[3] McDonough, G. F., Murphree, W. D., Blair, J. C., Scoggins, J. R., Reed, T. G., Linsley, E. L., Verderaime, V. S., Lovingood,

J. A., Rheinfurth, M. H., and Ryan, R. S., "Wind Effects on Launch Vehicles," Monograph AG115, The Advisory Group for Aerospace Research and Development (AGARD), NATO, Feb. 1970. Ed. by E. D. Geissler.

[4] Harpold, J. C., and Gavert, D. E., "Space Shuttle Entry Guidance Performance Results," *Journal of Guidance, Control, and Dynamics*, Vol. 6, No. 6, 1983, pp. 442–447. doi:10.2514/3.8523.

[5] Mendeck, G., and Craig, L., "Entry Guidance for the 2011 Mars Science Laboratory Mission," *AIAA Atmospheric Flight Mechanics Conference*, American Institute of Aeronautics and Astronautics, Portland, Oregon, 2011. doi:10.2514/6.2011-6639.

[6] Calhoun, P. C., and Queen, E. M., "Entry Vehicle Control System Design for the Mars Science Laboratory," *Journal of Spacecraft and Rockets*, Vol. 43, No. 2, 2006, pp. 324–329. doi:10.2514/1.19650.

[7] Kluever, C. A., "Entry Guidance Performance for Mars Precision Landing," *Journal of Guidance, Control, and Dynamics*, Vol. 31, No. 6, 2008, pp. 1537–1544. doi:10.2514/1.36950.

[8] Seiff, A., and Kirk, D. B., "Structure of the Atmosphere of Mars in Summer at Mid-Latitudes," *Journal of Geophysical Research*, Vol. 82, No. 28, 1977, pp. 4364–4378. doi:10.1029/JS082i028p04364.

[9] Kass, D. M., Schofield, J. T., Michaels, T. I., Rafkin, S. C. R., Richardson, M. I., and Toigo, A. D., "Analysis of Atmospheric Mesoscale Models for Entry, Descent, and Landing," *Journal of Geophysical Research: Planets*, Vol. 108, No. E12, 2003. doi:10.1029/2003JE002065.

[10] Seiff, A., "Mars Atmospheric Winds Indicated by Motion of the Viking Landers during Parachute Descent," *Journal of Geophysical Research: Planets*, Vol. 98, No. E4, 1993, pp. 7461–7474. doi:10.1029/92JE02738.

[11] Ferri, F., Smith, P. H., Lemmon, M., and Rennó, N. O., "Dust Devils as Observed by Mars Pathfinder," *Journal of Geophysical Research: Planets*, Vol. 108, No. E12, 2003. doi:10.1029/2000JE001421.

[12] Ding, Z., Zhou, H., Wang, F., Wu, D., Wu, Y., and He, Y., "An Implementation of the Cubature Kalman Filter for Estimating Trajectory Parameters and Air Data of a Hypersonic Vehicle," *Proceedings of the Institution of Mechanical Engineers, Part G: Journal of Aerospace Engineering*, 2019. doi:10.1177/0954410019835977.

[13] Pruett, C. D., Wolf, H., Heck, M. L., and Siemers, P. M., III, "Innovative Air Data System for the Space Shuttle Orbiter," *Journal of Spacecraft and Rockets*, Vol. 20, No. 1, 1983, pp. 61–69. doi:10.2514/3.28357.

[14] Baumann, E., Pahle, J. W., Davis, M. C., and White, J. T., "X-43A Flush Airdata Sensing System Flight-Test Results," *Journal of Spacecraft and Rockets*, Vol. 47, No. 1, 2010, pp. 48–61. doi:10.2514/1.41163.

[15] Artz, E. J., Dona, N. W., and Yechout, T. R., "NASA Orion Flush Air Data Sensing System Feasibility Determination and Development," *52nd Aerospace Sciences Meeting*, American Institute of Aeronautics and Astronautics, National Harbor, Maryland, 2014. doi:10.2514/6.2014-1115.

[16] Karlgaard, C. D., Kutty, P., and Schoenenberger, M., "Coupled Inertial Navigation and Flush Air Data Sensing Algorithm for Atmosphere Estimation," *AIAA Atmospheric Flight Mechanics Conference*, American Institute of Aeronautics and Astronautics, Kissimmee, Florida, 2015. doi:10.2514/6.2015-0526.

[17] Rhudy, M. B., Gu, Y., Gross, J. N., and Chao, H., "Onboard Wind Velocity Estimation Comparison for Unmanned Aircraft Systems," *IEEE Transactions on Aerospace and Electronic Systems*, Vol. 53, No. 1, 2017, pp. 55–66. doi: 10.1109/TAES.2017.2649218.

[18] Myschik, S., Heller, M., Holzapfel, F., and Sachs, G., "Low-Cost Wind Measurement System For Small Aircraft," *AIAA Guidance, Navigation, and Control Conference and Exhibit*, American Institute of Aeronautics and Astronautics, Providence, Rhode Island, 2004. doi:10.2514/6.2004-5240.

[19] Langelaan, J. W., Alley, N., and Neidhoefer, J., "Wind Field Estimation for Small Unmanned Aerial Vehicles," *Journal of Guidance, Control, and Dynamics*, Vol. 34, No. 4, 2011, pp. 1016–1030. doi:10.2514/1.52532.

[20] Petrich, J., and Subbarao, K., "On-Board Wind Speed Estimation for UAVs," *AIAA Guidance, Navigation, and Control Conference*, American Institute of Aeronautics and Astronautics, Portland, Oregon, 2011. doi:10.2514/6.2011-6223.

[21] Hollenbeck, D., Nunez, G., Christensen, L. E., and Chen, Y., "Wind Measurement and Estimation with Small Unmanned Aerial Systems (sUAS) Using On-Board Mini Ultrasonic Anemometers," *2018 International Conference on Unmanned Aircraft Systems (ICUAS)*, IEEE, Dallas, TX, 2018, pp. 285–292. doi:10.1109/ICUAS.2018.8453418.

[22] Hajiyev, C., Cilden-Guler, D., and Hacizade, U., "Two-Stage Kalman Filter for Estimation of Wind Speed and UAV Flight Parameters Based on GPS/INS and Pitot Tube Measurements," *9th International Conference on Recent Advances in Space Technologies (RAST)*, IEEE, Istanbul, Turkey, 2019, pp. 875–880. doi:10.1109/RAST.2019.8767886.

[23] McBride, D. D., and Sherman, P. M., "Pitot Pressure in Hypersonic Flow with Condensation." *AIAA Journal*, Vol. 9, No. 12, 1971, pp. 2354–2357. doi:10.2514/3.6518.

[24] Stephenson, W. B., "Use of Pitot Tube in Very Low Density Flows," Technical Report AEDC-TR-81-11, Arnold Engineering Development Center, Arnold AFB, Tennessee, 1981.

[25] Lee, J. H., Dogan, A., and Hullender, D., "Estimation of Aircraft States and Wind Exposure," *AIAA Atmospheric Flight Mechanics Conference*, American Institute of Aeronautics and Astronautics, Portland, Oregon, 2011. doi:10.2514/6.2011-6318.

[26] Hong, H., Wang, M., Holzapfel, F., and Tang, S., "Fast Real-Time Three-Dimensional Wind Estimation for Fixed-Wing Aircraft," *Aerospace Science and Technology*, Vol. 69, 2017, pp. 674–685. doi:10.1016/j.ast.2017.07.019.

[27] Donnell, G. W., Feight, J. A., Lannan, N., and Jacob, J. D., "Wind Characterization Using Onboard IMU of sUAS," *2018 Atmospheric Flight Mechanics Conference*, American Institute of Aeronautics and Astronautics, Atlanta, Georgia, 2018. doi:10.2514/6.2018-2986.

[28] McClelland, H. G., and Woolsey, C. A., "Effects of Model Simplification on Wind Reconstruction During Open-Loop Longitudinal Flight," *AIAA Scitech 2019 Forum*, American Institute of Aeronautics and Astronautics, San Diego, California, 2019. doi:10.2514/6.2019-1599.

[29] Chapman, G. T., and Kirk, D. B., "A Method for Extracting Aerodynamic Coefficients from Free-Flight Data," *AIAA Journal*, Vol. 8, No. 4, 1970, pp. 753–758. doi:10.2514/3.5752.

[30] Dutta, S., Braun, R. D., Russell, R. P., Striepe, S. A., and Clark, I. G., "Comparison of Statistical Estimation Techniques for Mars Entry, Descent, and Landing Reconstruction," *Journal of Spacecraft and Rockets*, Vol. 50, No. 6, 2013, pp. 1207–1221. doi:10.2514/1.A32459.

[31] Kazemba, C. D., Braun, R. D., Schoenenberger, M., and Clark, I. G., "Dynamic Stability Analysis of Blunt-Body Entry Vehicles Using Time-Lagged Aftbody Pitching Moments," *Journal of Spacecraft and Rockets*, Vol. 52, No. 2, 2015, pp. 393–403. doi:10.2514/1.A32894.

[32] Jegede, O., Fujita, K., Nagai, H., and Tanno, H., "Development of Free Flight Experimental and Analytical Procedures for Atmospheric Entry Vehicles," *AIAA Scitech 2019 Forum*, American Institute of Aeronautics and Astronautics, San Diego, California, 2019. doi:10.2514/6.2019-0019.

[33] Karlgaard, C., Beck, R., O'Keefe, S., Siemers, P., White, B., Engelund, W., and Munk, M., "Mars Entry Atmospheric Data System Modeling and Algorithm Development," *41st AIAA Thermophysics Conference*, American Institute of Aeronautics and Astronautics, San Antonio, Texas, 2009. doi:10.2514/6.2009-3916.

[34] Karlgaard, C. D., Beck, R. E., Derry, S. D., Brandon, J. M., Starr, B. R., Tartabini, P. V., and Olds, A. D., "Ares I-X Trajectory Reconstruction: Methodology and Results," *Journal of Spacecraft and Rockets*, Vol. 50, No. 3, 2013, pp. 641–661. doi:10.2514/1.A32345.

[35] Whitmore, S., Davis, R., and Fife, J., "In-Flight Demonstration of a Real-Time Flush Airdata Sensing (RT-FADS) System," *20th Atmospheric Flight Mechanics Conference*, American Institute of Aeronautics and Astronautics, Baltimore, Maryland, 1995. doi:10.2514/6.1995-3433.

[36] Cobleigh, B., Whitmore, S., Haering, E., Jr., Borrer, J., and Roback, V., "Flush Airdata Sensing (FADS) System Calibration Procedures and Results for Blunt Forebodies," *9th International Space Planes and Hypersonic Systems and Technologies Conference*, American Institute of Aeronautics and Astronautics, Norfolk, Virginia, 1999. doi:10.2514/6.1999-4816.

[37] Srivastava, A., Meade, A., and Long, K., "Learning Airdata Parameters for Flush Air Data Sensing Systems," *AIAA Infotech@Aerospace Conference*, American Institute of Aeronautics and Astronautics, Seattle, Washington, 2009. doi: 10.2514/6.2009-1938.

[38] Dahlhaus, R., "Maximum Likelihood Estimation and Model Selection for Locally Stationary Processes," *Journal of Nonparametric Statistics*, Vol. 6, No. 2-3, 1996, pp. 171–191. doi:10.1080/10485259608832670.

[39] Withers, P., and Catling, D., "Production of Reduced Data Records for the Phoenix Atmospheric Structure Experiment," LID urn:nasa:pds:phx_ase:document:report, NASA Planetary Data System, 2008.

[40] Karlgaard, C. D., and Tynis, J. A., "Mars Phoenix EDL Trajectory and Atmosphere Reconstruction Using NewSTEP," Technical Memorandum NASA/TM–2019–220282, Analytical Mechanics Associates, Inc., Hampton, Virginia, 2019.

[41] Justh, H. L., "Mars Global Reference Atmospheric Model 2010 Version: Users Guide," Technical Memorandum NASA/TM-2014-217499, NASA Marshall Space Flight Center, Huntsville, Alabama, 2014.

[42] Berman, Z., and Powell, J., "The Role of Dead Reckoning and Inertial Sensors in Future General Aviation Navigation," *IEEE 1998 Position Location and Navigation Symposium (Cat. No.98CH36153)*, IEEE, Palm Springs, California, 1998, pp. 510–517. doi:10.1109/PLANS.1998.670206.

[43] Groves, P. D., *Principles of GNSS, Inertial, and Multisensor Integrated Navigation Systems*, 2nd ed., GNSS Technology and Application Series, Artech House, Boston, 2013. OCLC: ocn820530994.

[44] Karlgaard, C. D., Kutty, P., Schoenenberger, M., Munk, M. M., Little, A., Kuhl, C. A., and Shidner, J., "Mars Science Laboratory Entry Atmospheric Data System Trajectory and Atmosphere Reconstruction," *Journal of Spacecraft and Rockets*, Vol. 51, No. 4, 2014, pp. 1029–1047. doi:10.2514/1.A32770.

[45] Karlgaard, C. D., Korzun, A. M., Schoenenberger, M., Bonfiglio, E., Kass, D., and Grover, M. R., "Mars InSight Entry, Descent, and Landing Trajectory and Atmosphere Reconstruction," *AIAA Scitech 2020 Forum*, American Institute of Aeronautics and Astronautics, Orlando, Florida, 2020. doi:10.2514/6.2020-1271.

[46] Schoenenberger, M., Hathaway, W., Yates, L., and Desai, P., "Ballistic Range Testing of the Mars Exploration Rover Entry Capsule," *43rd AIAA Aerospace Sciences Meeting and Exhibit*, American Institute of Aeronautics and Astronautics, Reno, Nevada, 2005. doi:10.2514/6.2005-55.

[47] Edquist, K. T., Desai, P. N., and Schoenenberger, M., "Aerodynamics for Mars Phoenix Entry Capsule," *Journal of Spacecraft and Rockets*, Vol. 48, No. 5, 2011, pp. 713–726. doi:10.2514/1.46219.

[48] Christian, J., Verges, A., and Braun, R., "Statistical Reconstruction of Mars Entry, Descent, and Landing Trajectories and Atmospheric Profiles," *AIAA SPACE 2007 Conference & Exposition*, American Institute of Aeronautics and Astronautics, Long Beach, California, 2007. doi:10.2514/6.2007-6192.

[49] Higgins, W., "A Comparison of Complementary and Kalman Filtering," *IEEE Transactions on Aerospace and Electronic Systems*, Vol. AES-11, No. 3, 1975, pp. 321–325. doi:10.1109/TAES.1975.308081.

[50] Euston, M., Coote, P., Mahony, R., Jonghyuk Kim, and Hamel, T., "A Complementary Filter for Attitude Estimation of a Fixed-Wing UAV," *2008 IEEE/RSJ International Conference on Intelligent Robots and Systems*, IEEE, Nice, France, 2008, pp. 340–345. doi:10.1109/IROS.2008.4650766.

[51] Yoo, T. S., Hong, S. K., Yoon, H. M., and Park, S., "Gain-Scheduled Complementary Filter Design for a MEMS Based Attitude and Heading Reference System," *Sensors*, Vol. 11, No. 4, 2011, pp. 3816–3830. doi:10.3390/s110403816.

[52] Ornik, M., and Topcu, U., "Learning and Planning for Time-Varying MDPs Using Maximum Likelihood Estimation," *arXiv:1911.12976 [cs.LG]*, 2019.

[53] Priestley, M. B., *Non-Linear and Non-Stationary Time Series Analysis*, Academic Press, London, UK, 1988.

[54] Boyd, S. P., and Vandenberghe, L., *Convex Optimization*, Cambridge University Press, Cambridge, UK, 2004.

[55] Hanger, M., Johansen, T. A., Mykland, G. K., and Skullestad, A., "Dynamic Model Predictive Control Allocation Using CVXGEN," *9th IEEE International Conference on Control and Automation (ICCA)*, IEEE, Santiago, Chile, 2011, pp. 417–422. doi:10.1109/ICCA.2011.6137940.

[56] Mattingley, J., and Boyd, S., "CVXGEN: A Code Generator for Embedded Convex Optimization," *Optimization and Engineering*, Vol. 13, No. 1, 2012, pp. 1–27. doi:10.1007/s11081-011-9176-9.

[57] Wright, S. J., *Primal-Dual Interior-Point Methods*, Society for Industrial and Applied Mathematics, 1997. doi:10.1137/1.9781611971453.

[58] Kouzoupis, D., Zanelli, A., Peyrl, H., and Ferreau, H. J., "Towards Proper Assessment of QP Algorithms for Embedded Model Predictive Control," *2015 European Control Conference (ECC)*, IEEE, Linz, Austria, 2015, pp. 2609–2616. doi:10.1109/ECC.2015.7330931.

[59] Withers, P., Towner, M., Hathi, B., and Zarnecki, J., "Analysis of Entry Accelerometer Data: A Case Study of Mars Pathfinder," *Planetary and Space Science*, Vol. 51, No. 9-10, 2003, pp. 541–561. doi:10.1016/S0032-0633(03)00077-1.

[60] McNeil Cheatwood, F., Bose, D., Karlgaard, C. D., Kuhl, C. A., Santos, J. A., and Wright, M. J., "Mars Science Laboratory (MSL) Entry, Descent, and Landing Instrumentation (MEDLI): Complete Flight Data Set," Technical Memorandum NASA-TM-2014-218533, NASA Langley Research Center, Hampton, Virginia, 2014.

[61] Hwang, H., Bose, D., Wright, H., White, T. R., Schoenenberger, M., Santos, J., Karlgaard, C. D., Kuhl, C., Oishi, T., and Trombetta, D., "Mars 2020 Entry, Descent, and Landing Instrumentation (MEDLI2)," *46th AIAA Thermophysics Conference*, American Institute of Aeronautics and Astronautics, Washington, D.C., 2016. doi:10.2514/6.2016-3536.

[62] Curtis, H. D., *Orbital Mechanics for Engineering Students*, Elsevier, 2020. doi:10.1016/C2016-0-02107-1.

[63] Desai, P. N., Prince, J. L., Queen, E. M., Schoenenberger, M. M., Cruz, J. R., and Grover, M. R., "Entry, Descent, and Landing Performance of the Mars Phoenix Lander," *Journal of Spacecraft and Rockets*, Vol. 48, No. 5, 2011, pp. 798–808. doi:10.2514/1.48239.

[64] Henderson, D. M., *Applied Cartesian Tensors for Aerospace Simulations*, American Institute of Aeronautics and Astronautics, 2006. doi:10.2514/4.861567.

[65] Ryne, M., Graat, E., Kruizinga, G., Lau, E., Martin-Mur, T., Nandi, S., Portock, B., Haw, R., and McElrath, T., "Orbit Determination for the 2007 Mars Phoenix Lander," *AIAA/AAS Astrodynamics Specialist Conference and Exhibit*, American Institute of Aeronautics and Astronautics, Honolulu, Hawaii, 2008. doi:10.2514/6.2008-7215.

[66] Konopliv, A. S., Asmar, S. W., Folkner, W. M., Karatekin, Ö., Nunes, D. C., Smrekar, S. E., Yoder, C. F., and Zuber, M. T., "Mars High Resolution Gravity Fields from MRO, Mars Seasonal Gravity, and Other Dynamical Parameters," *Icarus*, Vol. 211, No. 1, 2011, pp. 401–428. doi:10.1016/j.icarus.2010.10.004.

[67] Blanchard, R. C., and Desai, P. N., "Mars Phoenix Entry, Descent, and Landing Trajestory and Atmosphere Reconstruction," *Journal of Spacecraft and Rockets*, Vol. 48, No. 5, 2011, pp. 809–822. doi:10.2514/1.46274.

[68] Magalhães, J. A., Schofield, J. T., and Seiff, A., "Results of the Mars Pathfinder Atmospheric Structure Investigation," *Journal of Geophysical Research: Planets*, Vol. 104, No. E4, 1999, pp. 8943–8955. doi:10.1029/1998JE900041.

[69] King-Hele, D., and Allan, R., "The Rotational Speed of the Upper Atmosphere," *Space Science Reviews*, Vol. 6, No. 2, 1966. doi:10.1007/BF00222595.

[70] Johansen, T. A., Cristofaro, A., Sorensen, K., Hansen, J. M., and Fossen, T. I., "On Estimation of Wind Velocity, Angle-of-Attack and Sideslip Angle of Small UAVs Using Standard Sensors," *2015 International Conference on Unmanned Aircraft Systems (ICUAS)*, IEEE, Denver, Colorado, 2015, pp. 510–519. doi:10.1109/ICUAS.2015.7152330.

[71] Anderson, J. D., *Fundamentals of Aerodynamics*, 6th ed., McGraw-Hill Series in Aeronautical and Aerospace Engineering, McGraw Hill Education, New York, New York, 2017.

[72] Anderson, J. D., *Hypersonic and High-Temperature Gas Dynamics*, 3rd ed., American Institute of Aeronautics and Astronautics, Inc., Washington, D.C., 2019. doi:10.2514/4.105142.

[73] Mulaert, J. (ed.), *Special Course on Capsule Aerothermodynamics*, No. 808 in AGARD Report, AGARD, Neuilly-sur-Seine, France, 1997. OCLC: 833086061.

[74] Reilly, R. J., "Program for an Improved Hypersonic Temperature-Sensing Probe," Contractor Report NASA-CR-186025, NASA Dryden Flight Research Center, Edwards AFB, California, Jun. 1993.

[75] Camacho, E. F., and Bordons, C., *Model Predictive Control*, Advanced Textbooks in Control and Signal Processing, Springer London, London, UK, 2007. doi:10.1007/978-0-85729-398-5.

[76] Box, G. E. P., Jenkins, G. M., Reinsel, G. C., and Ljung, G. M., *Time Series Analysis: Forecasting and Control*, fifth edition ed., Wiley Series in Probability and Statistics, John Wiley & Sons, Inc., Hoboken, New Jersey, 2016.

[77] Ljung, L., and Söderström, T., *Theory and Practice of Recursive Identification*, No. 4 in The MIT Press Series in Signal Processing, Optimization, and Control, MIT Press, Cambridge, Massachusetts, 1983.

[78] Dzhaparidze, K., *Parameter Estimation and Hypothesis Testing in Spectral Analysis of Stationary Time Series*, Springer Series in Statistics, Springer New York, New York, New York, 1986. doi:10.1007/978-1-4612-4842-2.

[79] Morelli, E., "In-Flight System Identification," *23rd Atmospheric Flight Mechanics Conference*, American Institute of Aeronautics and Astronautics, Boston, Massachusetts, 1998. doi:10.2514/6.1998-4261.

[80] Billings, S. A., *Nonlinear System Identification: NARMAX Methods in the Time, Frequency, and Spatio-Temporal Domains*, John Wiley & Sons, Inc, Chichester, UK, 2013.

[81] Ifeachor, E. C., and Jervis, B. W., *Digital Signal Processing: A Practical Approach*, 2nd ed., Prentice Hall, Harlow, UK, 2002.

[82] Haber, R., Bars, R., and Schmitz, U., *Predictive Control in Process Engineering: From the Basics to the Applications*, Wiley-VCH Verlag GmbH & Co. KGaA, Weinheim, Germany, 2011. doi:10.1002/9783527636242.

[83] Nason, G. P., "Stationary and Non-Stationary Time Series," *Statistics in Volcanology*, edited by H. M. Mader, S. G. Coles, C. B. Connor, and L. J. Connor, The Geological Society of London on behalf of The International Association of Volcanology and Chemistry of the Earth's Interior, 2006, 1st ed., pp. 129–142. doi:10.1144/IAVCEI001.11.

[84] Priestley, M. B., "Evolutionary Spectra and Non-Stationary Processes," *Journal of the Royal Statistical Society. Series B. Methodological*, Vol. 27, 1965, pp. 204–237.

[85] Bierman, G. J., *Factorization Methods for Discrete Sequential Estimation*, No. v. 128 in Mathematics in Science and Engineering Series, Academic Press, New York, New York, 1977.

[86] Justus, C., Duvall, A., and Kller, V. W., "Engineering-Level Model Atmospheres for Titan and Mars," *Planetary Probe Atmospheric Entry and Descent Trajectory Analysis and Science*, Vol. 544, 2004, pp. 311–316.